CHAPTER 1
Introduction to the basic concepts

The goal of the first chapter is to introduce some of the key concepts required to understand the seismoelectric theory that will be developed for the saturated case in Chapter 2 and for the partially saturated and two-phase flow cases in Chapter 3. These key concepts include the electrical double layer theory and the reasons why an electrical (streaming) current density is produced when the pore water flows relative to the skeleton formed by the solid grains. In the context of the seismoelectric theory, the propagation of seismic waves will be responsible for the relative flow of pore water, and the resulting source current density will be responsible for electromagnetic (EM) disturbances. We will provide a short history of the seismoelectric method as well as its basic concepts. We will also give an introduction to wave propagation theory. At the end of this chapter, we will also provide some simulations using a simplified version of the seismoelectric theory that is based on the acoustic approximation. These models will illustrate, in a simple way, the key concepts behind the seismoelectric method, especially the difference between coseismic signals and seismoelectric conversions. Finally, we will present a preliminary model of seismoelectric phenomena pertaining to the Biot–Frenkel theory of linear poroelasticity.

1.1 The electrical double layer

As discussed later in Section 1.4, the existence of seismoelectric effects is closely related to the existence of the electrical double layer at the interface between the pore water and the skeleton (made of the elastic minerals). In the presence of several immiscible fluids in the pore space, seismoelectric effects can be also associated with the existence of an electrical double layer at the interface between the pore water and these other fluids such as air or oil. Therefore, we believe that it is important to start this book with an extensive description of what the electrical double layer is for silica and clay minerals that are in contact with an electrolyte composed of water molecules and ions. We will focus on silica and clays but the electrical double layer theory has been also developed for carbonates (Cicerone et al., 1992; Strand et al., 2006; Hiorth et al., 2010) and other types of aluminosilicates such as zeolites (van Bekkum et al., 2001).

The electrical double layer is a generic name given to electrochemical disturbances existing at the surface of minerals in contact with water containing dissolved ions. The electrical double layer comprises (1) the Stern layer of sorbed ions on the mineral surface (Stern, 1924) and (2) the diffuse layer of ions bound to the surface through the coulombic force associated with the deficiency or excess of electrical charges on the mineral surface and the Stern layer (Gouy, 1910; Chapman, 1913). The sorbed ions of the Stern layer possess a specific affinity for the mineral surface in addition to the coulombic interaction (specific is usually used to include all types of interactions that are not purely coulombic). In the case of the diffuse layer, the ions are interacting with the mineral surface only through the coulomb interaction.

The readers that are interested to understand the seismoelectric effect but that are not interested by the

The Seismoelectric Method: Theory and Applications, First Edition. André Revil, Abderrahim Jardani, Paul Sava and Allan Haas.

interfacial electrochemistry can skip Sections 1.1.1 and 1.1.2 and can go directly to Section 1.1.3 of this chapter.

1.1.1 The case of silica

1.1.1.1 A simplified approach

Figure 1.1 sketches the surface of a silica grain coated by an electrical double layer. When a mineral like silica is in contact with water, its surface becomes charged due to chemical reactions between the available surface bonding and the pore water as shown in Figure 1.2. For instance, the silanol groups, shown by the symbol >SiOH, of the surface of silica (where > refers to the mineral crystalline framework), behave as weak acid–base (amphoteric sites). This means that they can lose a proton when in contact with water to generate negative surface sites ($>SiO^-$). They can also gain protons to become positive sites ($>SiOH_2^+$). Putting water in contact with a fresh silica surface leads to a slight acidification of the pore water, as shown in Figure 1.2, which explains why silica is considered to be an acidic rock. At the opposite end, a mineral like carbonate will generate a basic pH (>7.0) in the pore water.

It follows that the mineral surface charge of silica appears to be pH dependent. It is typically negative at near-neutral pH values (pH 5–8) and possibly positive or neutral for very acidic conditions (pH <3). The simplest complexation reactions at the surface of silica can be summarized as (e.g., Wang & Revil, 2010, and references therein)

$$>SiOH + H^+ \Leftrightarrow >SiOH_2^+ \quad K_{(+)}, \tag{1.1}$$

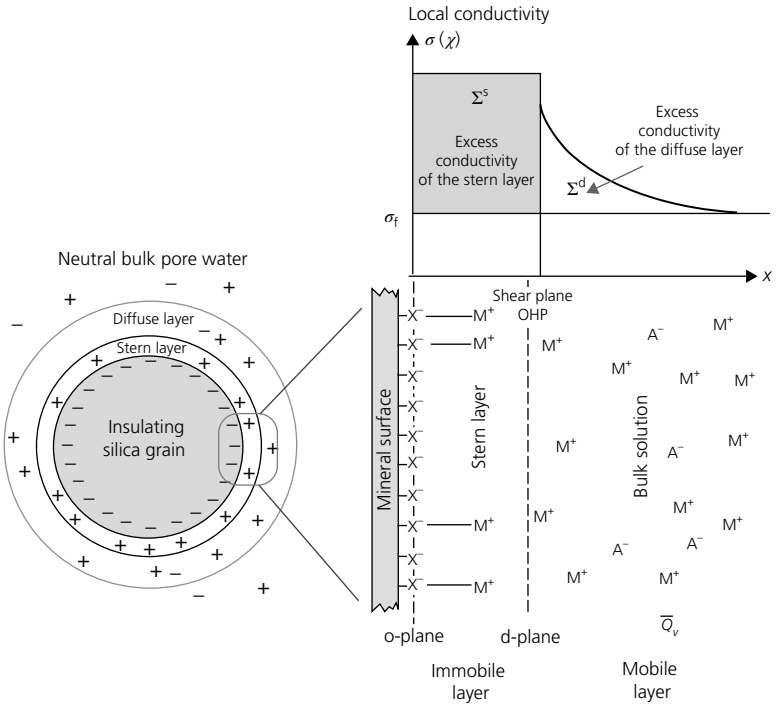

Figure 1.1 Sketch of the electrical double layer at the pore water–mineral interface coating a spherical grain (modified from Revil & Florsch, 2010). The local conductivity $\sigma(\chi)$ depends on the local distance χ from the charged surface of the mineral. The pore water is characterized by a volumetric charge density $\overline{Q}_V$ corresponding to the (total) charge of the diffuse layer per unit pore volume (in coulombs (C) m^{-3}). The Stern layer is responsible for the excess surface conductivity Σ^S (in siemens, S) with respect to the conductivity of the pore water σ_f, while the diffuse layer is responsible for the excess surface conductivity Σ^d. These surface conductivities are sometimes called specific surface conductance because of their dimension, but they are true surface conductivities. The Stern layer is comprised between the o-plane (mineral surface) and the d-plane, which is the inner plane of the electrical diffuse layer (OHP stands for outer Helmholtz plane). The diffuse layer extends from the d-plane into the pores. The element M^+ stands for the metal cations (e.g., sodium, Na^+), while A^- stands for the anions (e.g., chloride, Cl^-). In the present case (negatively charged mineral surface), M^+ denotes the counterions, while A^- denotes the coions. The fraction of charge contained in the Stern layer with respect to the total charge of the double layer is called the partition coefficient *f*.

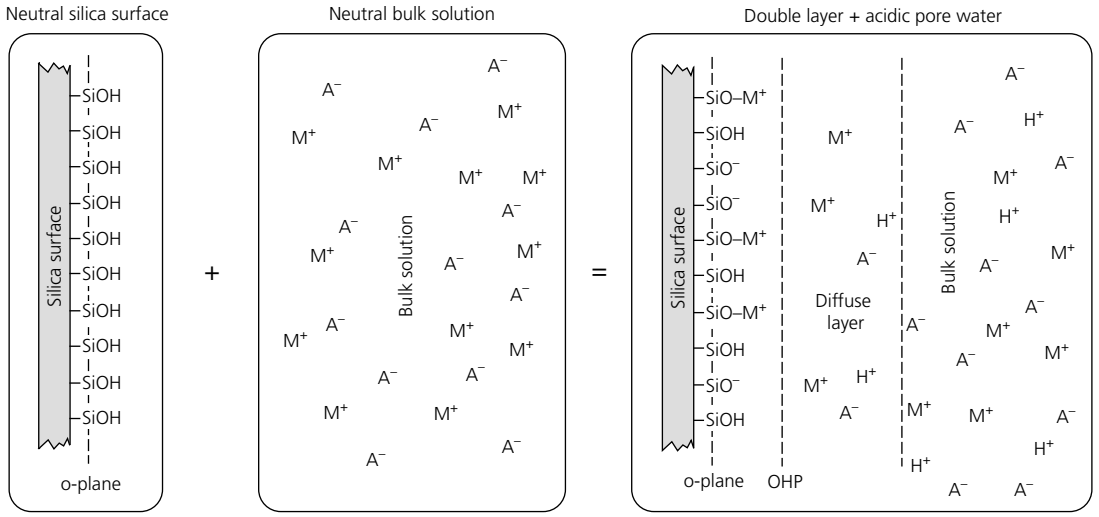

Figure 1.2 Formation of the electrical double layer in the case of silica. In the present case, a neutral silica surface is brought in contact with a neutral pore water solution composed of cations M^+ and anions A^-. The silanol surface groups at the surface of silica release a certain number of protons in the pore water, making the solution slightly acidic. Some of the cations from the pore water are adsorbed in the Stern layer. The surface charge density and the Stern layer charge density are compensated in the diffuse layer. In a sandstone, the bulk pore water is neutral (no net charge density), and only the diffuse layer is not neutral and more precisely characterized usually by an excess of (positive) charges.

$$>\mathrm{SiOH} \Leftrightarrow >\mathrm{SiO^-} + \mathrm{H^+} \quad K_{(-)}, \tag{1.2}$$

$$>\mathrm{SiOH} + \mathrm{M^+} \Leftrightarrow >\mathrm{SiO^-M^+} + \mathrm{H^+}, \quad K_{\mathrm{M}}, \tag{1.3}$$

where $K_{(\pm)}$ are the two equilibrium constants associated with the surface sorption and desorption of protons. This 2-pK model considers that two charged surface species, namely, $>SiO^-$ and $>SiOH_2^+$, are responsible for the surface charge density of silica. That said, the reaction in Equation (1.1) is often neglected in a number of studies because the occurrence of the positive sites, $>SiOH_2^+$, can only happen at low pH values (typically below pH <3 as mentioned briefly previously).

We also assume that the pore water contains a completely dissociated monovalent salt (e.g., NaCl providing the same amount of cations Na^+ and anions Cl^-). In the following, a "counterion" is an ion that is characterized by a charge opposite to the charge of the mineral surface, while a "coion" has a charge of the same sign as the mineral surface. The typical case for silica is to have a negative surface charge, and therefore, the counterions are the Na^+ cations and the coions are the Cl^- anions. Note however that the sorption of cations is characterized by a high valence and a strong affinity for the silica surface (for instance, Al^{3+}) and can reverse the charge of the mineral surface (surface and Stern later together) and therefore can reverse the sign of the charge of the diffuse layer. The sorption is described by the following reaction:

where K_{M} corresponds to the equilibrium constant for this reaction. Sorption is distinct from precipitation, which involves the formation of covalent bonds with the mineral surface. This sorption can be strong (formation of an inner-sphere complexes with no mobility along the mineral surface) or weak. In the "weak case," the formation of the Stern layer is a kind of condensation effect demonstrated by molecular dynamics. A weak sorption example is the case of a hydrated sodium. In this example, the sorbed counterion Na^+ keeps its hydration sphere, and it forms a so-called outer-sphere complex with the mineral surface (e.g., Tadros & Lyklema, 1969). Such counterions are expected to keep some mobility along the mineral surface, responsible (as briefly explained in Section 1.3) for a low-frequency polarization of the mineral grains in an alternating electrical field. The layer of ions formed by the sorption of these counterions directly on the mineral surface is called the Stern layer. The Stern layer is therefore located between the o-plane (mineral surface) and the d-plane, which is the inner plane of the electrical diffuse layer (Figures 1.1 and 1.2). The sorption of counterions occurs at the "β-plane" which is located in between the o- and d-planes shown in Figure 1.1.

As stated earlier, at near-neutral pH values, the surface charge of silica is generally negative. This negative surface attracts the ions of positive sign (counterions) and repels the ions of the same sign (coions). The surface charge that is not balanced by the sorption of some counterions in the Stern layer is balanced further away in the so-called diffuse layer. In normal conditions, the diffuse layer is therefore characterized by an excess of counterions and a depletion of coions with respect to the free pore water located in the central part of the pores (Figures 1.1 and 1.2). This concept of a diffuse layer was first developed by Gouy (1910) and Chapman (1913). The term "electrical double layer" is a generic name describing this electrochemical system coating the surface of the minerals and comprising of the Stern and the diffuse layers. The term electrical "triple layer model" (TLM) is often used in electrochemistry when different types of sorption phenomena are considered at the level of the Stern layer. In this case and as briefly discussed previously, electrochemists use the term "inner-sphere complexes" for ions strongly bound to the mineral surface (e.g., Cu^{2+} or NH_4^+ on the surface of silica). The term "outer-sphere complex" is used to characterize ions that are weakly bound to the mineral surface (e.g., K^+, Na^+) and generally keep their hydration layer and a certain mobility along the mineral surface. We will return later in this section to the idea of a strong sorption mechanism.

Electrokinetic properties are defined by measurable macroscopic effects associated with the relative displacement of the diffuse layer with respect to the solid phase, with the Stern layer attached to it (e.g., von Smoluchowski, 1906). One of the key parameters to define electrokinetic properties is the zeta potential. For simplicity, we assume that the zeta potential is the inner potential of the diffuse layer. Our goal is to define a simple model to determine the value of the zeta potential as a function of the pore water salinity for a simple 1:1 solution like NaCl or KCl. The availability of the different sites is obtained by solving one continuity equation for the surface sites and two constitutive equations based on reactions (1.2) and (1.3) earlier. These three equations are given by

$$\Gamma_S^0 = \Gamma_{SiOH}^0 + \Gamma_{SiO^-}^0 + \Gamma_{SiOM}^0, \tag{1.4}$$

$$K_{(-)} = \frac{\Gamma_{SiO}^0 - \alpha_{H^+}^0}{\Gamma_{SiOH}^0}, \tag{1.5}$$

$$K_M = \frac{\Gamma_{SiOM}^0 \alpha_{H^+}^0}{\Gamma_{SiOH}^0 \alpha_{M^+}^0}, \tag{1.6}$$

where Γ_i^0 corresponds to the number of sites i per surface area and $\alpha_{H^+}^0$ and $\alpha_{M^+}^0$ denote the activity of the protons and cations M^+ on the outer Helmholtz plane (OHP; see Figure 1.1). Equation (1.4) expresses the fact that the sum of all the different types of surface sites is equal to the crystalline site density Γ_S^0 of silanol groups on the surface of the grains. The value of this quantity can be determined from crystallographic considerations. The total site density Γ_S^0 is typically between 5 and 10 sites per nm^2.

Equations (1.5) and (1.6) represent the balance between species associated with the constitutive chemical reactions (1.2) and (1.3) assuming thermodynamic equilibrium for these reactions (kinetics is neglected) and assuming that reaction (1.1) can be safely neglected for near-neutral pH values. According to Revil et al. (1999a), we have $pK_{(-)} = -\log_{10} K_{(-)}$ is typically around 7.4–7.5 at 25°C and $pK_{Na^+} = -\log_{10} K_{Na^+}$ is typically close to 3.3 at 25°C, while $pK_{K^+} = -\log_{10} K_{K^+}$ is close to 2.8 at 25°C.

The solution of Equations (1.4)–(1.6) is straightforward and given by

$$\Gamma_{SiO^-}^0 = \frac{K_{(-)} \Gamma_S^0}{A \alpha_{H^+}^0}, \tag{1.7}$$

$$\Gamma_{SiOM}^0 = \frac{K_M \Gamma_S^0 \alpha_{M^+}^0}{\alpha_{H^+}^0 A}, \tag{1.8}$$

where the quantity A is defined by

$$A = 1 + \frac{K_{(-)}}{\alpha_{H^+}^0} + \alpha_{M^+}^0 \frac{K_M}{\alpha_{H^+}^0}. \tag{1.9}$$

Since, in this simplified model, there is only one type of charged site on the surface of the mineral, the surface charge density (charge per surface are of the mineral surface) is simply given by

$$Q_0^S = -e \Gamma_{SiO^-}^0, \tag{1.10}$$

where e is the elementary charge (1.6×10^{-19} C, C for coulomb).

The next step is to determine the equivalent surface charge density of the diffuse layer, which is characterized by an electrostatic potential that decreases away from the mineral surface $\varphi(\chi)$ where χ denotes the local distance away from the mineral surface assuming to be locally

smooth. The activity or concentrations of the ions in the electrical diffuse layer are determined through the use of Poisson–Boltzmann statistics. To understand these distributions, we need to define the so-called electrochemical potentials of cations (+) and anions (–). These electrochemical potentials are defined by (e.g., Gouy, 1910; Hunter, 1981)

$$\mu_i = \mu_i^0 + k_b T \ln \alpha_i + q_i \varphi, \tag{1.11}$$

where $\mu_{(\pm)}^0$ is the chemical potential of the ions in a reference state (a constant), k_b is the Boltzmann constant, T is temperature (in degrees K, Kelvin), α_i is the activity of species i (equal to the concentrations for dilute solutions), q_i is the charge of species i (in C; for instance, $q_{(+)} = e$ for Na^+ where e denotes the elementary charge 1.6×10^{-19} C), and φ is the electrostatic potential (in volts, V).

Local thermodynamic equilibrium between the electrical diffuse layer and the bulk pore water is given by the equality of the electrochemical potentials. We can consider equilibrium between a position χ away from the OHP (see position in Figure 1.1) and an arbitrary position in the bulk pore water for which the local potential of the electrical diffuse layer φ vanishes ($\varphi(\infty) = 0$). For monovalent ions, the condition (Hunter, 1981)

$$\mu_i(\chi) = \mu_i(\infty) \tag{1.12}$$

yields

$$\mu_i^0 + k_b T \ln \alpha_i(\chi) \pm e\varphi(\chi) = \mu_i^0 + k_b T \ln \alpha_i^f. \tag{1.13}$$

In Equation (1.13), $\alpha_{(\pm)}^f$ denotes the activity of the cations (+) or anions (–) far from the mineral surface and taken in the bulk pore water (in the bulk pore fluid, characterized by superscript f). It follows that the ionic activity of species i at the position of the OHP itself, α_i^0, is given as a function of the activity in the bulk pore water α_i^f by

$$\alpha_i^0 = \alpha_i^f X^{2q_i}, \tag{1.14}$$

$$X = \exp\left(-\frac{\varphi_d}{2k_b T}\right), \tag{1.15}$$

where φ_d denotes the electrical potential at the OHP (i.e., the inner plane of the electrical diffuse layer). The charge in the diffuse layer is given by averaging the concentrations over the thickness of the electrical diffuse layer. In the general case, the charge density in the diffuse layer is given by

$$Q_S = \int_0^\infty \sum_{i=1}^N q_i C_i(\chi) d\chi \tag{1.16}$$

$$Q_S = \sum_{i=1}^N q_i \int_0^\infty C_i^f \exp\left(-\frac{q_i \varphi(\chi)}{k_b T}\right) d\chi. \tag{1.17}$$

We have also the useful property (Pride, 1994)

$$\int_0^\infty \exp\left(-\frac{q_i \varphi(\chi)}{k_b T}\right) d\chi = 2\chi_d \exp\left(-\frac{q_i \varphi_d}{2k_b T}\right), \tag{1.18}$$

where $2\chi_d$ represents an average thickness for the diffuse layer ($\chi_d = (\varepsilon_f k_b T / 2e^2 C_f)^{1/2}$ where e denotes the elementary charge 1.6×10^{-19} C, k_b denotes the Boltzmann constant, and ε_f denotes the dielectric constant of water). The length scale χ_d is called the Debye screening length in electrical double layer theory (e.g., Gouy, 1910, Chapman, 1913). From Equations (1.17) and (1.18), we obtain

$$Q_S = 2\chi_d \sum_{i=1}^N q_i C_i^f X^{q_i}. \tag{1.19}$$

The potential in the diffuse layer is approximately given by the Debye formula $\varphi(\chi) = \varphi_d \exp(-\chi/\chi_d)$ (e.g., Pride, 1994) where φ_d denotes the local potential on the OHP. For a binary symmetric 1:1 electrolyte, the expression of the charge density of the diffuse layer reduces to (using Eq. 1.15)

$$Q_S = \sqrt{aC_f} \sinh\left(\frac{-\varphi_d}{2k_b T}\right), \tag{1.20}$$

$$a = 8 \times 10^3 \varepsilon_f k_b T N, \tag{1.21}$$

where N denotes the Avogadro number (6.0221×10^{23} mol^{-1}). We can rewrite the charge density of the diffuse layer as

$$Q_S = \frac{1}{2}\sqrt{aC_f}\left(X - \frac{1}{X}\right). \tag{1.22}$$

The electrical double layer problem can be finally solved by using a final condition in the form of a global electroneutrality condition for the electrical double layer and the mineral surface. This condition implies that the

charge density on the mineral surface is exactly counterbalanced by the charge density in the Stern layer and the charge density in the diffuse layer. In order to get an analytical solution for the zeta potential, we are going to omit the charge density in the Stern layer (a fair approximation for silica but not for clays). It follows that the total electroneutrality condition can be written as

$$Q_S + Q_0^S = 0. \tag{1.23}$$

Using Equations (1.7), (1.10), (1.14), and (1.22) into Equation (1.23), the potential of the Stern layer φ_d is the solution of the following equation:

$$\alpha\left(X - \frac{1}{X}\right)\left(1 + \beta X^2\right) - 1 = 0, \tag{1.24}$$

where

$$\alpha = \frac{\sqrt{aC_f}}{2e\Gamma_S^0}, \tag{1.25}$$

$$\beta = \frac{10^{-pH} + K_M C_f}{K_{(-)}}, \tag{1.26}$$

and where X is defined by Equation (1.15) and a by Equation (1.21). At low salinities, we have $X \gg (1/X)$. With this assumption, Equation (1.24) simplified to the following cubic equation:

$$X^3 + pX + q = 0, \tag{1.27}$$

with $p = 1/\beta$ and $q = -1/(\alpha\beta)$. The real root of this cubic equation is given by

$$X = \left(-\frac{q}{2} + \sqrt{\Delta}\right)^{1/3} + \left(-\frac{q}{2} - \sqrt{\Delta}\right)^{1/3}, \tag{1.28}$$

where

$$\Delta = \left(\frac{q}{2}\right)^2 + \left(\frac{p}{3}\right)^3 = \frac{1}{4\alpha^2\beta^2} > 0 \tag{1.29}$$

(assuming $4\alpha^2/(27\beta) \ll 1$, which can be easily checked). Using Equation (1.15), the solution is simply given by

$$\varphi_d = \frac{2k_bT}{3e}\ln(\alpha\beta). \tag{1.30}$$

In electrokinetic properties, the zeta potential represents the electrical potential of the diffuse layer at the position of the hydrodynamic shear plane, which is defined as the position of zero relative velocity between the solid and liquid phases. The exact position of the zeta potential is unknown but likely pretty close to the mineral surface. If we assume that the zeta potential represents the potential on the OHP (see Figure 1.1 for the position of this plane), it follows from Equation (1.30) that we can write the zeta potential as (Revil et al., 1999a, b)

$$\zeta = b\log_{10}C_f + c, \tag{1.31}$$

where

$$b = \frac{k_bT}{3e}\ln 10, \tag{1.32}$$

$$c = \frac{2k_bT}{3e}\ln\left[\frac{(8\times10^3\varepsilon_f k_bTN)^{1/2}}{2eK_{(-)}\Gamma_S^0}10^{-pH}\right]. \tag{1.33}$$

This equation shows how the zeta potential depends on the salinity C_f for simple supporting 1:1 electrolytes. Note that Pride and Morgan (1991, their Figure 4) came to Equation (1.31) on purely empirical grounds, fitting experimental data with such an equation and getting empirically the values of b and c. Typically, the seismoelectric community has been using Equation (1.31) only as an empirical equation while it can derived from physical grounds as demonstrated by Revil et al. (1999a). The previous model yields $b = 20$ mV per tenfold change in concentration (salinity) for a 1:1 electrolyte. A comparison between the prediction of Equation (1.31) and a broad dataset of experimental data is shown in Figure 1.3. The slope b of the experimentally determined zeta potential is actually closer to 24 mV per tenfold change in concentration, therefore fairly close to the predicted value.

Equation (1.31) is not valid at very high salinities (10^{-1} mol l^{-1} and above). Jaafar et al. (2009) presented measurements of the streaming potential coupling coefficient in sandstone core samples saturated with NaCl solutions at concentrations up to 5.5 mol l^{-1} (Figure 1.3). Using measurement of the streaming potential coupling coefficient, they were able to determine the zeta potential up to the saturated concentration limit in salinity. They found that the magnitude of the zeta potential also decreases with increasing salinity, as discussed previously and as predicted by Equation (1.31), but approaches a constant value at high salinity around −20 mV. This value is, so far, not captured by exiting models.

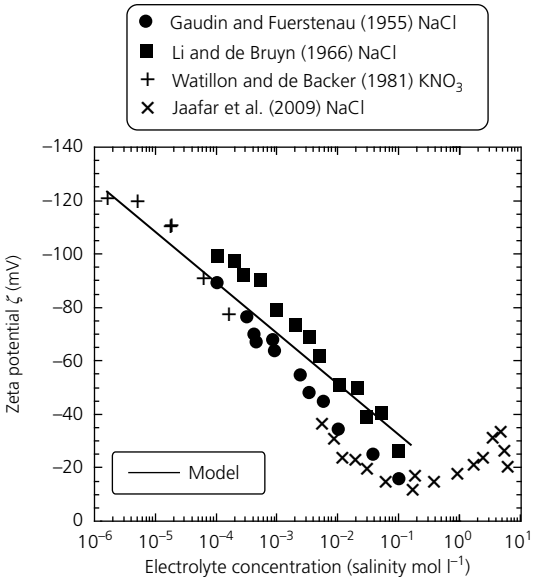

Figure 1.3 Zeta potential ζ on the surface of a silica grain. Comparison between the analytical model developed in the main text (plain line, Eqs. 1.31–1.33) and experimental data from the literature. These data are from Gaudin and Fuerstenau (1955), Li and De Bruyn (1966), Watilllon and De Backer (1970), and Jaafar et al. (2009). We use pH = 5.6 (pH of pure water in equilibrium with the atmosphere), $K_{(-)} = 10^{-7.4}$, and a density of surface active site at the surface of silica of $\Gamma_S^0 = 7$ sites nm^{-2}. Note the high salinity values are not captured by the model.

Table 1.1 Equilibrium constants for surface complexes at the surface of a silica sand.

Reactions	Equilibrium constants
$>SiOH + H^+ \leftrightarrow > SiOH^{2+}$	$10^{-2.2}$
$>SiOH \leftrightarrow > SiO^- + H^+$	$10^{-6.2}$
$>SiO^- + Na^+ \leftrightarrow >SiO^-\ Na^+$	$10^{-4.5}$
$>SiOH + Cu^{2+} \leftrightarrow >SiOCu^+ + H^+$	$10^{-3.4}$
$2 > SiOH + Cu^{2+} \leftrightarrow 2(>SiO)^-Cu^{2+} + 2H^+$	$10^{-8.8}$
$>SiOH + SO_4^{2-} + H^+ \leftrightarrow >SiSO_4^- + H_2O$	$10^{5.0}$

From Sverjensky (2005).

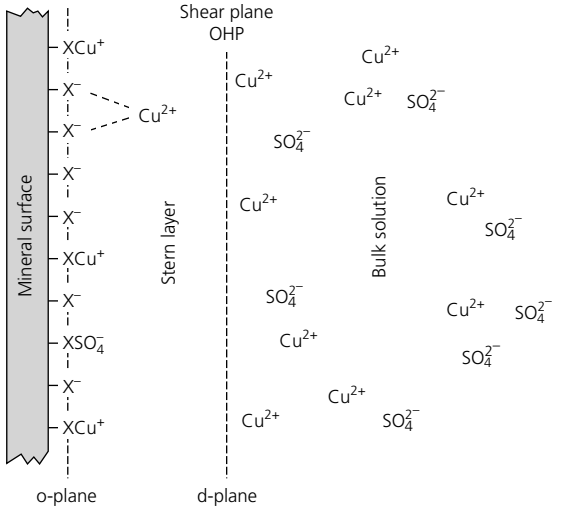

Figure 1.4 Sketch of the electrical double layer showing the speciation of copper and sulfate for a solution of copper sulfate in contact with a silica surface. Sorption of copper on the mineral surface (inner-sphere ligand) occurs as a monodentate complex (immobile), while sorption in the Stern layer (outer-sphere ligand) occurs as a (mobile) bidentate complex. This type of sorption has a strong effect on the value of the zeta potential and can, under given conditions, reverse the polarity of the zeta potential on the surface of silica. The o-plane denotes the mineral surface, and the d-plane denotes the outer Helmholtz plane (OHP) on which the zeta potential ζ is considered.

In addition, the analysis made earlier is correct only for silica in contact with simple supporting electrolytes such as NaCl or KCl with a weak sorption of the counterions. As mentioned briefly previously, the composition of the pore water can, however, strongly influence the value and even the sign of the zeta potential. In the case of strong sorptions, it is necessary to account for more intricate complexation reactions on the surface of silica like the one shown in Table 1.1 for copper. Figure 1.4 shows the speciation of copper on the mineral surface forming both monodentate and bidentate complexes. In the presence of such strong sorption phenomena, the zeta potential can reverse sign and drastically change in magnitude. This is especially true in the case of the sorption of cations of high valence (e.g., Al^{3+}) directly on the mineral surface. In such inner-sphere complex, the cation loses part of the hydration layer. The charge density of the counterions in the Stern layer can be high enough to overcome the charge density on the surface of the mineral. In this case, the charge of the diffuse layer and its associated zeta potential have a reversed polarity, at a given pH, with respect to what is normal for a simple supporting binary electrolyte like NaCl or KCl. Electrokinetic phenomena like the seismoelectric effect are very sensitive to these types of chemical changes because they are directly controlled by the properties of the electrical double layer and by the zeta potential.

1.1.1.2 The general case

A complete electrical double layer model for silica is now discussed avoiding most of the assumption used previously. The drawbacks of such approach, however, are that there are no analytical solutions of the system of equation and we have to use a numerical approach to determine the zeta potential and the surface charge for a given set of environmental conditions. We consider again silica grains in contact with a binary symmetric electrolyte like NaCl for the simplicity of the presentation and comparison with the experimental data. In the pH range 4–10, the surface mineral reactions at the silanol surface sites can be written as

$$>SiO^- + H^+ \Leftrightarrow >SiOH, \quad K_1, \tag{1.34}$$

$$>SiOH + H^+ \Leftrightarrow >SiOH_2{}^+, \quad K_2, \tag{1.35}$$

$$>SiO^- + Na^+ \Leftrightarrow >SiONa, \quad K_3. \tag{1.36}$$

The symbol ">" refers to the mineral framework, and K_1, K_2, K_3 are the associated equilibrium constants for the different reactions reported earlier (see Table 1.1). Additional reactions for a multicomponent electrolyte can be easily incorporated by adding reactions similar to Equation (1.36) or exchange reactions. Therefore, the present model is not limited to a binary salt. The protonation of surface siloxane groups $>SiO_2$ is extremely low, and these groups can be considered as inert. We neglect here the adsorption of anion Cl^- at the surface of the $>SiOH_2{}^+$ sites which occurs at pH < pH (pzc) ≈ 3, where pzc denotes the point of zero charge of silica:

$$\mathrm{pH(pzc)} = \frac{1}{2}(\log K_1 + \log K_2). \tag{1.37}$$

Consequently, the value of K_2 is determined from the value of K_1 and pH (pzc) ≈ 3. The surface charge density Q_0 (in C m^{-2}) at the surface of the minerals can be expressed as follows:

$$Q_0 = e\left(\Gamma^0_{SiOH_2} - \Gamma^0_{SiO} - \Gamma^0_{SiONa}\right), \tag{1.38}$$

where Γ^0_i denotes the surface site density of species i (in sites m^{-2}). The surface charge density Q_β in the Stern layer is determined according to

$$Q_\beta = e\Gamma^0_{SiONa}. \tag{1.39}$$

The surface charge density in the diffuse layer is calculated using the classical Gouy–Chapman relationship in the case of a symmetric monovalent electrolyte:

$$Q_S = -\sqrt{8\epsilon k_b T C_f}\sinh\left(\frac{e\varphi_d}{2k_bT}\right), \tag{1.40}$$

where C_f is the salinity in the free electrolyte (in mol l^{-1}), T is the temperature (in K), ε_f is the permittivity of the pore water ($\varepsilon_f = 81\ \varepsilon_0$, $\varepsilon_0 \sim 8.85 \times 10^{-12}$ F m^{-1}), e represents the elementary charge (taken positive, $e = 1.6 \times 10^{-19}$ C), and k_b is the Boltzmann constant (1.381×10^{-23} J K^{-1}). The electrical potential φ_d (in V) is the electrical potential at the OHP (see Figure 1.1). We make again the assumption that the electrical potential φ_d is equal to the zeta potential ζ placed at the shear plane. The shear plane is the hydrodynamic surface on which the relative velocity between the mineral grains and the pore water is null.

The continuity equation for the surface sites yields

$$\Gamma^0_1 = \Gamma^0_{SiO} + \Gamma^0_{SiOH} + \Gamma^0_{SiOH_2} + \Gamma^0_{SiONa}, \tag{1.41}$$

where Γ^0_1 (in sites m^{-2}) is the total surface site density of the mineral. We use the equilibrium constants associated with the half reactions to calculate the surface site densities Γ^0_i. Solving Equation (1.41) with the expressions of the equilibrium constants defined through Equations (1.34)–(1.36) yields

$$\Gamma^0_{SiO} = A\Gamma^0_1, \tag{1.42}$$

$$\Gamma^0_{SiOH} = A\Gamma^0_1 K_1 C^f_{H^+}\exp\left(-\frac{e\varphi_0}{k_bT}\right), \tag{1.43}$$

$$\Gamma^0_{SiOH_2{}^+} = A\Gamma^0_1 K_1 K_2 C^{f}_{H^+}{}^2\exp\left(-\frac{2e\varphi_0}{k_bT}\right), \tag{1.44}$$

$$\Gamma^0_{SiONa} = A\Gamma^0_1 K_3 C^f_{Na^+}\exp\left(-\frac{e\varphi_\beta}{k_bT}\right), \tag{1.45}$$

$$A = 1 + K_1 C^f_{H^+}\exp\left(-\frac{e\varphi_0}{k_bT}\right) + K_1K_2C^{f}_{H^+}{}^2\exp\left(-\frac{2e\varphi_0}{k_bT}\right) + K_3 C^f_{Na^+}\exp\left(-\frac{e\varphi_\beta}{k_bT}\right), \tag{1.46}$$

where φ_0 and φ_β are, respectively, the electrical potential at the o-plane corresponding to the mineral surface and the electrical potential at the β-plane corresponding to

the plane of the Stern layer (see Figure 1.1). The electrical potentials φ_0, φ_β, and φ_d are related by

$$\varphi_0 - \varphi_\beta = \frac{Q_0}{C_1}, \tag{1.47}$$

$$\varphi_\beta - \varphi_d = -\frac{Q_S}{C_2}, \tag{1.48}$$

where C_1 and C_2 (in F m^{-2}) are the (constant) integral capacities of the inner and outer parts of the Stern layer, respectively. The global electroneutrality equation for the mineral/water interface is

$$Q_0 + Q_\beta + Q_S = 0. \tag{1.49}$$

We calculate the φ_d potential—thanks to Equations (1.38)–(1.49)—using an iterative method to solve the system of equations. We use $\Gamma_1^0 = 5$ sites m^{-2} and $C_2 = 0.2$ F m^{-2}. We use the values of K_1, K_3, and C_1 reported in Figure 1.5 to calculate the surface charge density Q_0 at the surface of silica mineral and the potential φ_d. The predictions of this double layer model are compared to the literature data (zeta potential and surface charge) in Figure 1.5. With the same model parameters, the surface charge of the mineral and the zeta potential can be described by this model as a function of the pH and salinity. Such type of model can also be used to predict the effect of specific sorption of cations like Cu^{2+} on the zeta potential/surface charge density of the silica surface.

As shown previously, the counterions are both located in the Stern and in the diffuse layer. The fraction of counterions located in the Stern layer is defined by

$$f = \frac{\Gamma^0_{SiONa}}{\Gamma^0_{SiONa} + \Gamma^D_{Na}}, \tag{1.50}$$

where the surface charge density of the counterions in the diffuse layer is given by

$$\Gamma^D_{Na} \equiv \int_0^\infty \left[C^D_{Na^+}(\chi) - C^f_{Na^+}\right] d\chi = C^f_{Na^+} \int_0^\infty \left\{ \exp\left[-\frac{e\varphi(\chi)}{k_b T}\right] - 1 \right\} d\chi \tag{1.51}$$

and the electrical potential in the diffuse layer φ is given by

$$\varphi(\chi) = \frac{4k_b T}{e} \tanh^{-1}\left[\tanh\left(\frac{e\varphi_d}{4k_b T}\right) \exp\left(-\frac{\chi}{\chi_d}\right)\right]. \tag{1.52}$$

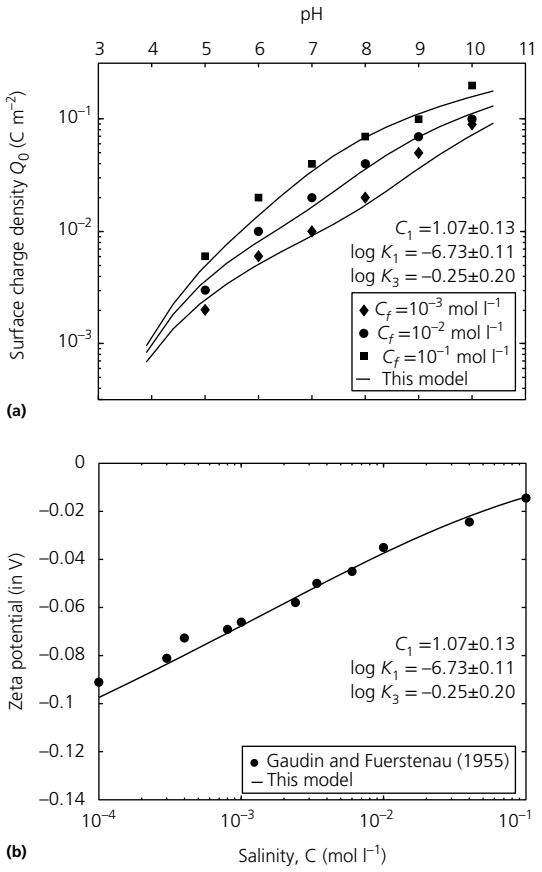

Figure 1.5 Comparison between the predictions of the triple layer model described in the main text at the end of Section 1.1 and experimental data in the case of silica. **a)** Comparison between the prediction of the model and surface charge density measurements obtained by potentiometric titrations at three different salinities (NaCl) and in the pH range 5–10 (Data from Kitamura et al., 1999). **b)** Comparison between the model prediction and measurements of the zeta potential at different salinities and pH = 6.5 (Data from Gaudin & Fuerstenau, 1955). The same model parameters are used for the two simulations.

In Equation (1.52), χ denotes the distance defined locally normal from the interface between the pore water and the solid grain, χ_d is the Debye screening length (in m), and Γ^D_{Na} is the equivalent surface density of the counterions in the diffuse layer. Figures 1.6 and 1.7 show that the fraction of counterions located in the Stern layer, f, depends strongly on the salinity and pH of the pore water solution. For example, at pH = 9 and at low salinities (≤10^{-3} mol l^{-1}), most of the counterions are located in

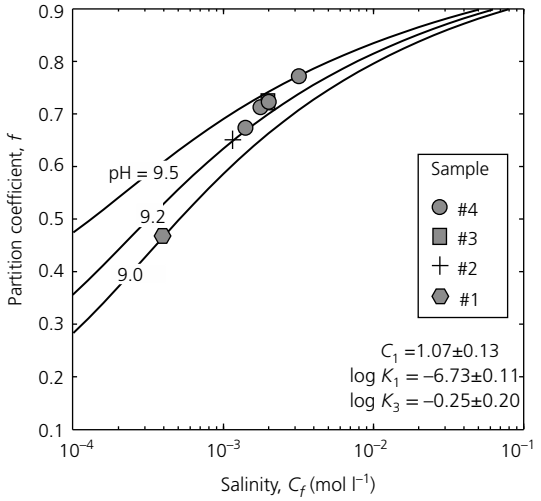

Figure 1.6 Partition coefficient versus the salinity of the free electrolyte with the TLM parameters indicated on Figure 1.2 for NaCl (pH = 9, 9.2, 9.5). The symbols correspond to the partition coefficient determined from the complex conductivity data for the seven experiments described in the main text. The data are determined from spectral induced polarization measurements (see Leroy et al., 2008). They show an increase of the partition coefficient with the salinity and the pH in fair agreement with the model.

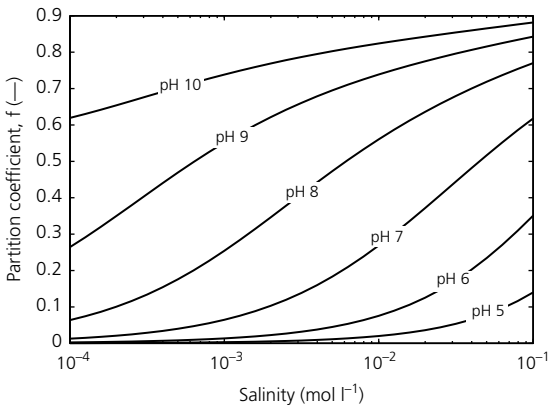

Figure 1.7 Determination of the partition coefficient though a triple layer model for silica for different values of the pH and salinity of NaCl solutions.

the diffuse layer, while at high salinity (>10^{-3} mol l^{-1}), the counterions are mostly located in the Stern layer.

1.1.2 The case of clays

Clays are ubiquitous in nature, and as such, their influence on electrical properties in general and the seismoelectric properties in particular is very important. A second reason to be interested by clays comes from their very small particle size (typically smaller than 5 μm) and the charged nature of their crystalline planes (Figure 1.8). The small size of the clay particles implies that they carry a huge charge per unit pore volume of porous rocks. There are at least two families of clay minerals depending on whether the space between the clay crystals is open or closed: on the one hand, kaolinite, chlorite, and illite have no open interlayer porosity, while on the other hand, smectite has an interlayer porosity strongly influencing its swelling properties. Figure 1.8 shows that the surface charge density of the clay particles has two distinct origins: one is located essentially on the basal planes that is mostly due to isomorphic substitutions in the crystalline framework and is pH independent (this charge is dominant for smectite). The second charge density is mostly located on the edge of the crystals due to amphoteric (pH-dependent) active sites.

The small particle size of clay minerals implies in turn a high specific surface area and a high cation exchange capacity (CEC) by comparison with other minerals. The specific surface area S_{sp} (in m^2 kg^{-1}) corresponds to the amount of surface area divided by the mass of grains. The CEC (in C kg^{-1}) corresponds to the amount of charge that can be titrated on the mineral surface divided by the mass of mineral. The ratio of the CEC by the specific surface area corresponds to the effective charge density on the mineral surface:

$$Q_0^S = \frac{\text{CEC}}{S_{sp}}. \tag{1.53}$$

As shown in Figure 1.9, the charge per unit surface is pretty constant for all clay minerals and comprised between 1 and 3 elementary charges per nm^2 at near-neutral pH values. Because part of the charge on the surface of the clay minerals is pH dependent, Maes et al. (1979) proposed for 3.9 ≤ pH ≤ 5.9 and for montmorillonite (a special type of smectite) the following pH-dependent relationship for the CEC: CEC (in meq g^{-1}) = 79.9 + 5.04 pH for monovalent cations and CEC (in meq g^{-1}) = 96.1 + 3.93 pH for divalent cations.

A theory for the electrical double layer of clay minerals is now introduced. This theory can be used to predict the amount of charge on the mineral surface and in the Stern layer or more directly the zeta potential. It can also be used to predict a highly important parameter used in

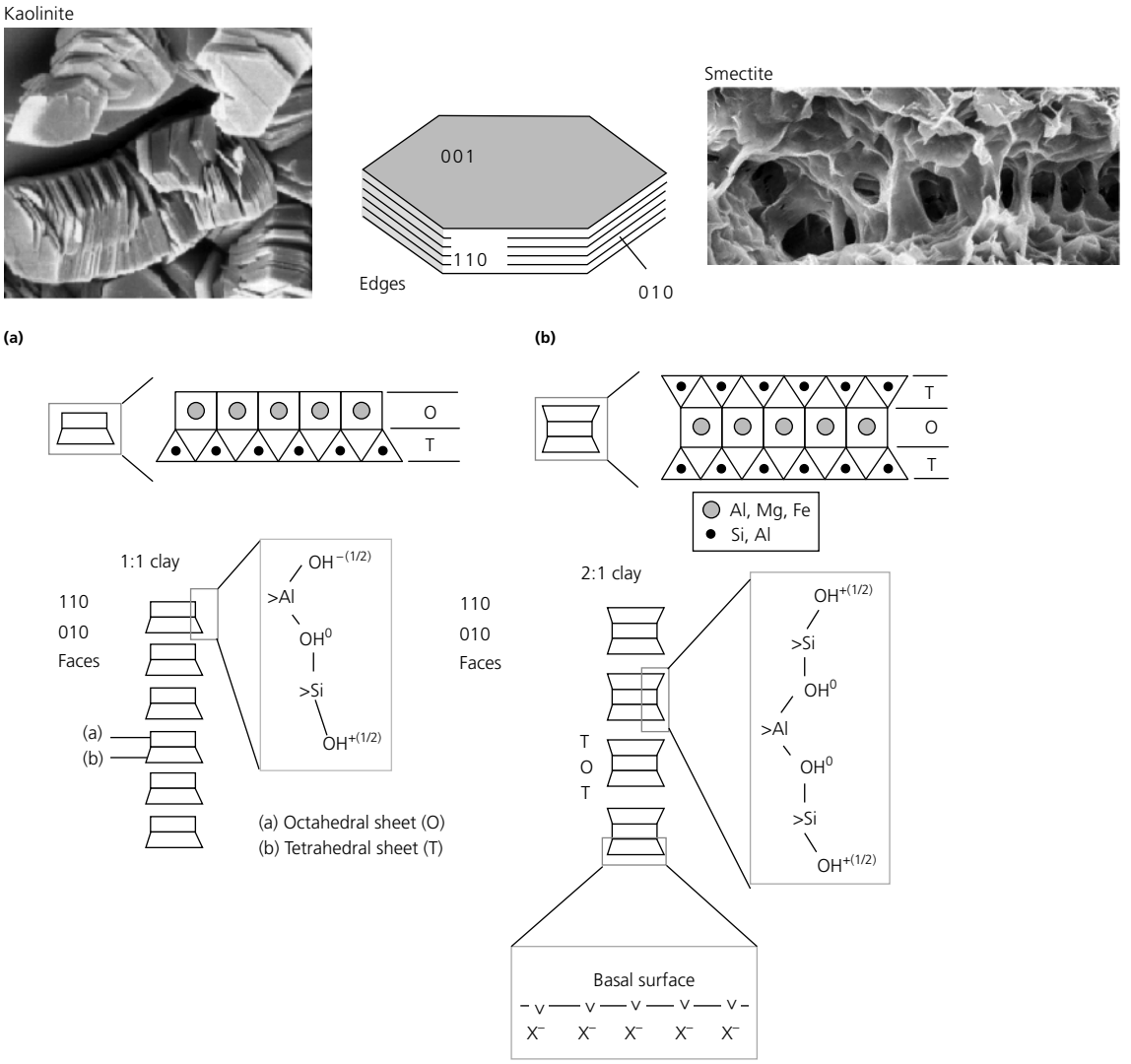

Figure 1.8 Active surface sites at the edge of **a)** 1:1 clays (kaolinite) and **b)** 2:1 clays (smectite or illite). In the case of kaolinite, the surface sites are mainly located on the edge of the mineral ({110} and {010} planes). In the case of smectite and illite and in the pH range near neutrality (5–9), the surface sites are mainly located on the basal plane ({001} plane), and they are due to isomorphic substitutions inside the crystalline framework (Modified from Leroy & Revil, 2004). Note also the difference in the morphology of the clay particles. T and O represent tetrahedral and octahedral sheets, respectively.

the determination of the complex conductivity of these minerals. This parameter is called the partition coefficient f (dimensionless). It describes the amount of counterions in the Stern layer by comparison with the total amount of counterions in the Stern and diffuse layers together.

We consider first a kaolinite crystal in contact with a binary symmetric electrolyte like NaCl. We restrict our analysis to the pH range 4–10, which is the pH range useful for most practical applications in geophysics. In this pH range and in the case of kaolinite, the surface mineral reactions at the aluminol, silanol, and >Al–O–Si< surface sites can be written as

$$>\mathrm{AlOH_2}^{1/2+} \Leftrightarrow >\mathrm{AlOH}^{1/2-} + \mathrm{H}^+, \quad K_1, \qquad (1.54)$$

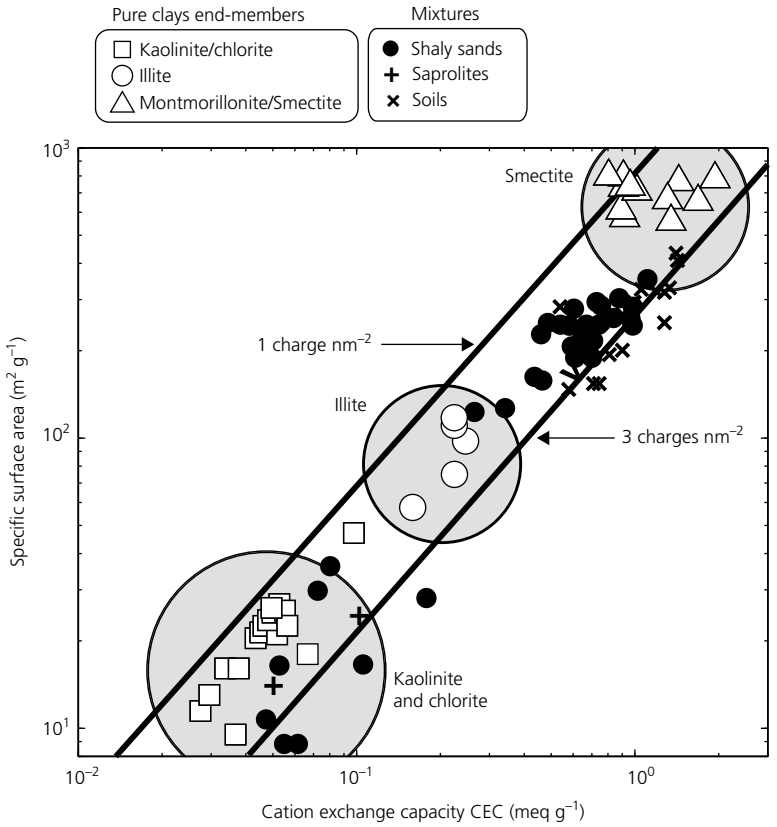

Figure 1.9 Specific surface area of clay minerals S_s (in $m^2\ g^{-1}$) as a function of the cation exchange capacity (CEC) (in meq g^{-1} with 1 meq g^{-1} = 96,320 C kg^{-1} in SI units) for various clay minerals. The ratio between the CEC and the specific surface area gives the equivalent total surface charge density of the mineral surface. The shaded circles correspond to generalized regions for kaolinite, illite, and smectite. The two lines correspond to 1–3 elementary charges per unit surface area. Data for the clay end members are from Patchett (1975), Lipsicas (1984), Zundel and Siffert (1985), Lockhart (1980), Sinitsyn et al. (2000), Avena and De Pauli (1998), Shainberg et al. (1988), Su et al. (2000), and Ma and Eggleton (1999). Saprolite data: Revil et al. (2013). Soil data: Chittoori and Puppala (2011).

$$>\mathrm{SiOH}^{1/2+} \Leftrightarrow\ >\mathrm{SiO}^{1/2-} + \mathrm{H}^+,\quad K_2, \tag{1.55}$$

$$>\mathrm{Al-ONa-Si}< \ \Leftrightarrow\ >\mathrm{Al-O}^- -\mathrm{Si}< + \mathrm{Na}^+,\quad K_3, \tag{1.56}$$

where K_1, K_2, and K_3 are the equilibrium constants of reactions (1.54)–(1.56) and the sign ">" refers to the crystalline framework. The surface site >Al–O–Si< carries a net (−1) negative charge (Avena & DePauli, 1998). We assume that the surface complexation reactions occur on the {010} and {110} planes of kaolinite.

The availability of the surface sites introduced by the chemical reactions described previously at the surface of the {010} and {110} planes can be described by the conservation equations for the three types of sites (aluminol, silanol, and >Al–O–Si< surface sites). Solving these equations, we obtain the concentrations of the different surface sites:

$$\Gamma^0_{\mathrm{AlOH}} = \frac{\Gamma^0_1}{A}, \tag{1.57}$$

$$\Gamma^0_{\mathrm{AlOH_2}} = \frac{\Gamma^0_1}{A}\left(\frac{C^{\mathrm{f}}_{\mathrm{H}^+}}{K_1}\right)\exp\left(-\frac{e\varphi_0}{k_{\mathrm{b}}T}\right), \tag{1.58}$$

$$\Gamma^0_{\mathrm{SiO}} = \frac{\Gamma^0_2}{B}, \tag{1.59}$$

$$\Gamma^0_{\mathrm{SiOH}} = \frac{\Gamma^0_2}{B}\left(\frac{C^{\mathrm{f}}_{\mathrm{H}^+}}{K_2}\right)\exp\left(-\frac{e\varphi_0}{k_{\mathrm{b}}T}\right), \tag{1.60}$$

$$\Gamma^0_{\mathrm{AlOSi}} = \frac{\Gamma^0_3}{C}, \tag{1.61}$$

$$\Gamma^0_{\mathrm{AlONaSi}} = \frac{\Gamma^0_3}{C}\left(\frac{C^{\mathrm{f}}_{\mathrm{Na}^+}}{K_3}\right)\exp\left(-\frac{e\varphi_\beta}{k_{\mathrm{b}}T}\right), \tag{1.62}$$

where A, B, and C are given by

$$A = 1 + \frac{C^{\mathrm{f}}_{\mathrm{H}^+}}{K_1}\exp\left(-\frac{e\varphi_0}{k_{\mathrm{b}}T}\right), \tag{1.63}$$

$$B = 1 + \frac{C^{\mathrm{f}}_{\mathrm{H}^+}}{K_2}\exp\left(-\frac{e\varphi_0}{k_{\mathrm{b}}T}\right), \tag{1.64}$$

$$C = 1 + \frac{C^{f}_{Na^+}}{K_3}\exp\left(-\frac{e\varphi_\beta}{k_b T}\right), \quad (1.65)$$

where e is the elementary charge (in C), T is the temperature (in degree K), k_b is the Boltzmann constant, Γ^0_i is the surface site density of site i, and Γ^0_1, Γ^0_2, Γ^0_3 (in sites per nm^2) are the total surface site densities of the three type of sites introduced earlier (aluminol, silanol, and >Al–O–Si< groups, respectively). The parameters C^f_i where $i = Na^+, H^+$ are the ionic concentrations (in mol l^{-1}), and φ_0 and φ_β are the electrical potentials at the mineral surface (o-plane) and at the β-plane, respectively (Figure 1.1). The resulting mineral surface charge density, Q_0, and the surface charge density in the Stern layer, Q_β (in C m^{-2}), are found by summing the surface site densities of charged surface groups (see Leroy & Revil, 2004).

In the case of smectite and illite, the surface site densities are located mainly on the basal plane {001} (Tournassat et al., 2004). We use the TLM developed by Leroy et al. (2007) to determine the distribution of the counterions at the mineral/water interface of 2:1 clay minerals. In the pH range 6–8, the influence of the hydroxyl surface sites upon the distribution of the counterions at the mineral/water interface can be neglected because the charge density induced by edge sites is small relative to that due to permanent excess of negative charge associated with the isomorphic substitutions inside the crystalline network of the smectite (Tournassat et al., 2004). We therefore consider only these sites in the model denoted as the "X-sites" (see Figure 1.8). The adsorption of sodium is described by

$$>XNa \Leftrightarrow\ >X^- + Na^+,\ \ K_4, \quad (1.66)$$

$$\Gamma^0_{XNa} = \Gamma^0_X\left(\frac{C^f_{Na^+}}{K_4}\right)\exp\left(-\frac{e\varphi_\beta}{k_b T}\right). \quad (1.67)$$

The mineral surface charge density Q_0 (in C m^{-2}) of smectite associated with these sites is considered equal to the ratio between the CEC of smectite (1 meq g^{-1}) and its specific surface area (800 m^2 g^{-1}), which gives a value equal to 0.75 charge nm^{-2} (for illite, a similar analysis yields 1.25 charges nm^{-2}). These values allow the calculation of the surface site densities Γ^0_X and Γ^0_{XNa} knowing the expressions of the mineral surface charge density Q_0 (in C m^{-2}) as a function of the surface site densities (see Leroy et al., 2007).

There are three distinct microscopic electric potentials in the inner part of the electrical layer. We note φ_0 as the mean potential on the surface of the mineral (Figure 1.1). The potential φ_β is located at the β-plane, and φ_d is the potential at the OHP (Figure 1.1). These potentials are related to each other by a classical capacitance model (Hunter, 1981):

$$\varphi_0 - \varphi_\beta = \frac{Q_0}{C_1}, \quad (1.68)$$

$$\varphi_\beta - \varphi_d = -\frac{Q_S}{C_2}, \quad (1.69)$$

where C_1 and C_2 (in F m^{-2}) are the (constant) integral capacities of the inner and outer parts of the Stern layer, respectively (Table 1.2). The parameter Q_S represents the surface charge density in the diffuse layer. The global electroneutrality equation for the mineral/water interface is

$$Q_0 + Q_\beta + Q_S = 0. \quad (1.70)$$

We calculate the potential φ_d by using Equations (1.68)–(1.70) and the procedure reported by Leroy and Revil (2004) and Leroy et al. (2007) (the surface charge densities are expressed as a function of the corresponding surface site densities). We use the values of the equilibrium constants K_i and of the capacities C_1 and C_2 reported in Table 1.2. The system of equations was solved inside two MATLAB routines, one for kaolinite and one for illite and smectite. The counterions are both located in the Stern and in the diffuse layer. For all clay minerals, the fraction of counterions located in the Stern layer is defined by Equations (1.50)–(1.52) like for the silica surface.

Table 1.2 Optimized double layer parameters for the three main types of clay minerals (at 25°C).

Parameters	Kaolinite	Illite	Smectite
K_1 (at 25°C)	10^{-10}*	—	—
K_2 (at 25°C)	8×10^{-6}*	—	—
K_3 (at 25°C)	5×10^{-2}*	—	—
K_4 (at 25°C)	—	0.8†	0.8†
C_1 (F m^{-2})	1.58*	1†	1†
C_2 (F m^{-2})	0.2*	0.2†	0.2†

* From Leroy and Revil (2004).
† From Leroy et al. (2007).

As shown by Leroy and Revil (2004) and Leroy et al. (2007), the previous set of equations can be solved numerically using the parameters given in Table 1.2 as input parameters. The parameters of Table 1.2 have been optimized from a number of experimental data, especially zeta potential resulting from electrokinetic measurements and surface conductivity data (see Leroy & Revil, 2004; Leroy et al., 2007), and remain unchanged in the present work. The output parameters of the numerical TLM are the surface site densities in the Stern and diffuse layers and therefore the partition coefficient f. Some TLM computations of the fractions of counterions in the Stern layer show that f is typically in the range 0.80–0.99, indicating that clay minerals have a much larger fraction of counterions in the Stern layer by comparison with glass beads at the same salinities. The values of the partition coefficient determined from the present model are also consistent with values determined by other methods, for instance, using radioactive tracers (Jougnot et al., 2009) and osmotic pressure (Gonçalvès et al., 2007; Jougnot et al., 2009). This shows that the present electrochemical model is consistent because it can explain a wide diversity of properties.

1.1.3 Implications

As discussed in Sections 1.1.1 and 1.1.2, all minerals of a porous material in contact with water are coated by the electrical double layer shown in Figure 1.1. The surface of the mineral is charged (due to isomorphic substitutions in the crystalline network or surface ionization of active sites such as hydroxyl >OH sites). The surface charge is balanced by charges located in the Stern layer and in the diffuse layer. There are three fundamental implications associated with the existence of this electrical double layer at the surface of silicates and clays:

1 Pore water is never neutral. There is an excess of charge in the pore water that can be written as

$$\bar{Q}_V = (1-f)\rho_g\left(\frac{1-\phi}{\phi}\right)\mathrm{CEC}, \tag{1.71}$$

where f denotes the fraction of counterions in the Stern layer (attached to the grains) and therefore $(1-f)$ denotes the fraction of charge contained in the diffuse layer, ρ_g denotes the mass density of the grains (kg m^{-3}), ϕ denotes the porosity, and CEC denotes the cation exchange capacity of the material (in C kg^{-1}). We will see later that the flow of the pore water relative to the grain framework drags an effective charge density $\hat{Q}_V^0$. We expect that for permeable porous media, we have

$$\hat{Q}_V^0 \ll \bar{Q}_V. \tag{1.72}$$

In sandstones, the diffuse layer is relatively thin with respect to the size of the pores and especially for the pores that controlled the flow of the pore water. In other words, most of the water is neutral with the exception of the pore water surrounding the surface of the grains. In addition, only a small fraction of the diffuse layer is carried along the pore water flow. We will see that the charge density $\hat{Q}_V^0$ should be understood as an effective charge density that is controlled by the flow properties (especially the permeability) and that has little to do with the CEC itself. It should be clear therefore that the CEC cannot be determined from the effective charge density $\hat{Q}_V^0$, which will be properly defined later.

2 There is an excess of electrical conductivity in the vicinity of the pore water–mineral interface responsible for the so-called surface conductivity (see Figure 1.1). This surface conductivity exists for any minerals in contact with water including clean sands. That said, the magnitude of surface conductivity is much stronger in the presence of clay minerals due to their very high surface area (surface area of the pore water–mineral interface for a given pore volume).

3 The double layer is responsible for the (nondielectric) low-frequency polarization of the porous material. This polarization is coming from the polarization of the electrical double layer in the presence of an electrical field applied to the porous material. In the case of seismoelectric effects, it implies a phase lag between the pore fluid pressure and the electric field, but this phase lag is expected to be small (typically <10 mrad except at very low salinities where the magnitude of the phase can reach 30 mrad) and most of the time is neglected (for instance, by Pride, 1994).

The first consequence is fundamental to understanding the nature of electrical currents associated with the flow of pore water relative to the mineral framework (termed streaming currents); therefore, the occurrence of electrokinetic (macroscopic) electrical fields is due to the flow of pore water relative to the mineral framework associated

with seismic waves. The second consequence is crucial to the understanding of electrical conductivity in porous materials. Electrical conductivity of porous media has two contributions, one associated with conduction in the bulk pore water and one associated with the electrical double layer (surface conductivity). Contrary to what is erroneously assumed in a growing number of scientific papers in hydrogeophysics, the formation factor will not be defined as the ratio of the conductivity of the pore water by the conductivity of the porous material. We will show that surface conductivity is crucial in obtaining an intrinsic formation factor characterizing the topology of the pore space of porous materials. The third consequence is important to the understanding of induced polarization, which translates into the frequency dependence of the electrical conductivity. Because of this low-frequency polarization, the conductivity appears, generally speaking, as a second-order symmetric tensor with components that are frequency dependent and complex. The real (or inphase) components are associated with electromigration, while the imaginary (quadrature) components are associated with polarization (i.e., the reversible storage of electrical charges in the porous material). We will show in the following that the model of Pride (1994) does not account correctly for the frequency dependence of electrical conductivity and is incomplete in its description of the electrical double layer (no speciation and no description of the Stern layer).

1.2 The streaming current density

We evaluate in this section the first consequence associated with the existence of the electrical double layer coating the surface of the mineral grains in a porous material. We have established in Section 1.1.1 that there is an excess charge density in pore water. We have defined the macroscopic charge density (charge per unit pore volume, in $C\,m^{-3}$) that is dragged by the flow of pore water as $\hat{Q}_V^0$ (the reason for the superscript 0 will be explored in Chapter 3). We showed that pore water, in proximity to the mineral grain surface, is characterized by a local charge density $\rho(\mathbf{x})$ (in $C\,m^{-3}$) at position $\mathbf{x}$ due to the presence of the electrical diffuse layer ($\rho(\mathbf{x}) = 0$ in the bulk pore water that is electroneutral). We note $\mathbf{v}_m(\mathbf{x})$ as the local instantaneous velocity of the pore water relative to the solid (in $m\,s^{-1}$). The macroscopic charge density $\hat{Q}_V^0$ is defined by

$$\hat{Q}_V^0 \langle \mathbf{v}_m(\mathbf{x}) \rangle = \langle \rho(\mathbf{x}) \mathbf{v}_m(\mathbf{x}) \rangle \tag{1.73}$$

where the brackets denote a pore volume averaging,

$$\langle \cdot \rangle = \frac{1}{V_p} \int_{V_p} (\cdot) d\tau, \tag{1.74}$$

and $d\tau$ denotes an elementary volume around point $M(\mathbf{x})$, and $\langle \mathbf{v}_m(\mathbf{x}) \rangle$ denotes the mean velocity averaged over the pore space. Equation (1.73) is valid whatever the size of the diffuse layer with respect to the size of the pores. In the case of a thin double layer (the thickness of the diffuse layer is much smaller than the thickness of the pores), the charge density $\hat{Q}_V^0$ is substantially smaller than the (total) charge density associated with the diffuse layer $\bar{Q}_V$, which explains why $\hat{Q}_V^0$ cannot be used to estimate the CEC of the minerals. In other words, there is no direct relationship between the effective charge density $\hat{Q}_V^0$ and the CEC of the minerals.

As shown in Figure 1.10, the drag of the excess of charge of the pore water (more precisely the drag of a fraction of the diffuse layer) is responsible for a macroscopic streaming source current density $\mathbf{J}_S$ at the scale of a representative elementary volume of the porous material. This macroscopic source density is related to the microscopic (pore scale) current density $\mathbf{j}_S$ associated with the local advective transfer of electrical charges by

$$\mathbf{J}_S = \phi \langle \mathbf{j}_S \rangle, \tag{1.75}$$

$$\mathbf{J}_S = \phi \langle \rho \mathbf{v}_m \rangle, \tag{1.76}$$

$$\mathbf{J}_S = \hat{Q}_V^0 \phi \langle \mathbf{v}_m \rangle, \tag{1.77}$$

$$\mathbf{J}_S = \hat{Q}_V^0 \dot{\mathbf{w}} \tag{1.78}$$

where $\dot{\mathbf{w}} = \phi \langle \mathbf{v}_m \rangle$ (Dupuit–Forchheimer equation) denotes the macroscopic Darcy velocity (in $m\,s^{-1}$; see Darcy, 1856). This Darcy velocity is not a true pore water velocity. It represents the flux of water through a cross section of the porous material (volume of water passing per surface area and per surface time across a cross section of the porous material). In Figure 1.10, we show the effect of the charge distribution and the flow regime on the source current density. At low frequencies, the flow is dominated by viscous effects, and the regime is called the viscous laminar flow regime. At high frequencies, the flow is controlled by the inertial term of the Navier–Stokes equation, and the flow regime is called

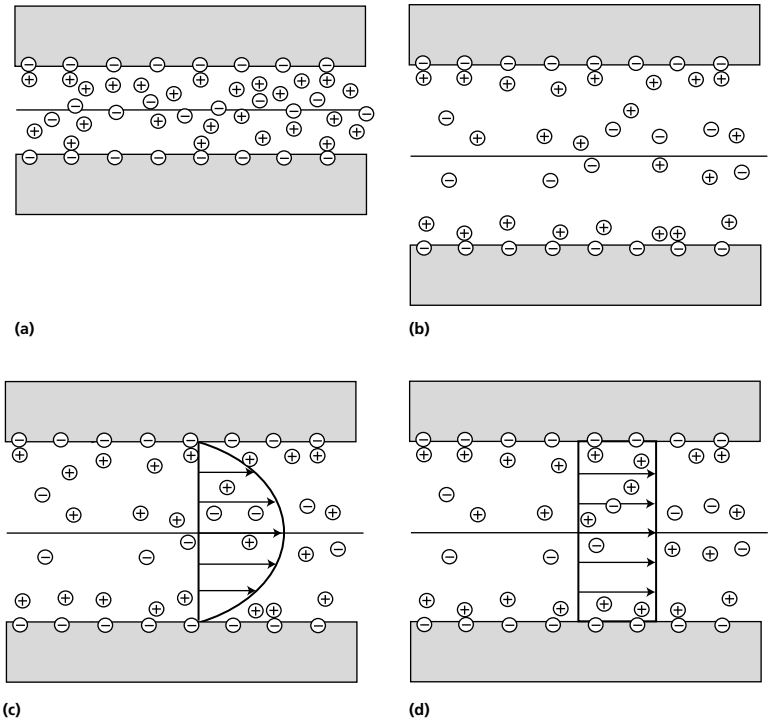

Figure 1.10 Sketch of the charge distribution and flow regime in a single pore. The grey areas correspond to the solid phase. There are four end members to consider depending on the pore size with respect to the double layer thickness and depending on the frequency. **a)** Thick double layer (the counterions of the diffuse layer are uniformly distributed in the pore space). **b)** Thin double layer (the thickness of the diffuse layer is much smaller than the size of the pores). **c)** Viscous laminar flow regime occurring at low frequencies. **d)** Inertial laminar flow regime occurring at high frequencies (Modified from Revil & Mahardika, 2013).

the inertial flow regime. This regime occurs for Reynolds numbers higher than 1 but smaller than the critical Reynolds number corresponding to turbulent flow (typically 200–300). For a broad range of porous media, the effective charge density, $\hat{Q}_V^0$, can be related directly to the permeability, k_0, as shown in Figure 1.11. This relationship is very useful to compute or invert the seismoelectric data since it offers a key relationship between the parameter that is controlling the seismoelectric coupling (as shown later) and the key hydraulic parameter of porous media, namely, the permeability.

The macroscopic source current density can be expressed directly as a function of the pore pressure gradient using Darcy's law. This law can be seen as a constitutive equation for the flow of the pore water at the scale of a representative elementary volume or can be seen as a macroscopic momentum conservation equation for the pore fluid. It is given by (Darcy, 1856)

$$\dot{\mathbf{w}} = -\frac{k_0}{\eta_f}\nabla p, \tag{1.79}$$

where η_f denotes the dynamic viscosity of the pore water (in Pa s), k_0 (in m^2) denotes the low-frequency permeability of the porous material, and p denotes the pore fluid (mechanical) pressure. Therefore, the streaming current density can be given by

$$\mathbf{J}_S = -\frac{\hat{Q}_V^0 k_0}{\eta_f}\nabla p. \tag{1.80}$$

A popular alternative that can be derived by volume averaging the Nernst–Planck equation is the macroscopic Helmholtz–Smoluchowski equation. For the streaming current density, it takes the following form (e.g., Pride, 1994):

$$\mathbf{J}_S = \frac{\varepsilon_f \zeta}{\eta_f F}\nabla p, \tag{1.81}$$

where F is called the electrical formation factor (dimensionless) and corresponds to a parameter that is properly defined in the modeling of the electrical conductivity of porous media (see Section 1.3). Equation (1.81) assumes a thin electrical double layer with respect to the size of the pores, while Equation (1.80) does not require such an assumption. A comparison between the two equations shows that the salinity dependence of $\hat{Q}_V^0$ should be the

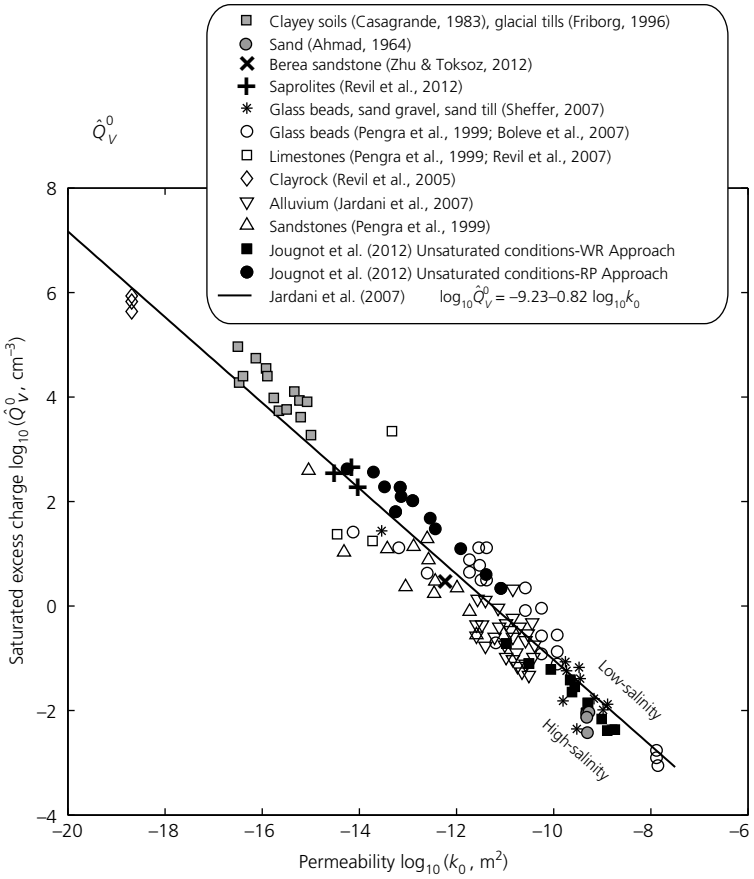

Figure 1.11 Quasistatic charge density $\hat{Q}_V^0$ (excess pore charge moveable by the quasistatic pore water flow) versus the quasistatic permeability k_0 for a broad collection of core samples and porous materials. This charge density is derived directly from laboratory measurements of the streaming potential coupling coefficient. Data from Ahmad (1969), Bolève et al. (2007), Casagrande (1983), Friborg (1996), Jougnot et al. (2012), Jardani et al. (2007), Pendra et al. (1999), Revil et al. (2005, 2007), Sheffer (2007), Revil et al. (2012), and Zhu and Toksöz (2013). The effective charge density $\hat{Q}_V^0$ cannot be used to predict the cation exchange capacity of the porous material. We also show the smaller effect of salinity.

same as the salinity dependence of the zeta potential, ζ. The polarity of $\hat{Q}_V^0$ is opposite to the polarity of ζ, and any change affecting the zeta potential would modify the effective charge density $\hat{Q}_V^0$ in the same way. A comparison between Equations (1.81) and (1.80) implies that at first approximation we have the following equivalence between the parameters: $\hat{Q}_V^0 k_0 \Leftrightarrow \varepsilon_f \zeta / F$.

1.3 The complex conductivity

In this section, we examine the second and third consequences associated with the electrical double layer, namely, the existence of surface conductivity and the existence of low-frequency polarization associated with the quadrature electrical conductivity. At low frequencies (below few kHz), porous media and colloids are not only conductive, but they store, reversibly, electrical charges (Marshall & Madden, 1959; Titov et al., 2004; Leroy et al., 2008; Grosse, 2009). The total current density $\mathbf{J}$ can be decomposed into a contribution associated with the electromigration of the charge carriers plus a contribution associated with the "true" polarization of the material:

$$\mathbf{J} = \sum_{i=1}^{N} q_i \mathbf{J}_i + \frac{\partial \mathbf{D}}{\partial t}, \tag{1.82}$$

where $\mathbf{J}_i$ denotes the flux density of species i (the number of species passing per unit surface area and per unit time) and $\mathbf{D}$ is the displacement field associated with dielectric polarization of the porous material. In nonequilibrium thermodynamics, the flux densities $\mathbf{J}_i$ are coupled to other transport mechanisms in the porous media. These ionic fluxes are directly controlled by the gradient of the electrochemical potentials, introduced in Section 1.1, and

the flow of pore water. These factors generate the source current density, $\mathbf{J}_S$, of electrokinetic origin. These couplings were first investigated by Marshall and Madden (1959) and imply the existence of low-frequency polarization mechanisms in the porous material. It is not our goal to develop a complete theory of polarization in this book, but rather to provide a practical view of the problem that can be used to analyze seismoelectric effects.

One of the most effective mechanisms of polarization is the coupling of the flux densities with the electrochemical potential gradients as discussed by Marshall and Madden (1959). The polarization implies a phase lag between the current and the electrical field and defines the frequency dependence of the conductivity of the material. Despite the fact that the seismoelectric theory contains an electroosmotic polarization effect (which is the one used by Pride (1994)), it has been known since Marshall and Madden (1959) that this mechanism cannot explain the low-frequency dependence of the conductivity of the material. While this assumption is clearly stated in Pride (1994), it seems to have been lost in translation in all the following works. In those works, the model of Pride is used to explain the low-frequency polarization of porous rocks, and as such, those authors have considered the mathematical expression of Pride (1994) as valid to describe the complex conductivity of porous materials. This is unfortunately not correct since the model of Pride does not account for low-frequency polarization mechanisms known to control the quadrature conductivity.

Continuing from the preceding text, the total current density entering, for instance, Ampère's law is

$$\mathbf{J} = \sigma^* \mathbf{E} + \mathbf{J}_S + \frac{\partial \mathbf{D}}{\partial t}, \tag{1.83}$$

where the first term on the right side of Equation (1.83) corresponds to a frequency-dependent electrical conductivity, σ^*, characterized by a real (inphase) component σ' and a quadrature (out-of-phase) component σ'':

$$\sigma^* = \sigma' + i\sigma'', \tag{1.84}$$

where i denotes the pure imaginary number $\left(i = \sqrt{-1}\right)$. The second term of Equation (1.83) corresponds to the source current density of electrokinetic origin, and the third term corresponds to the displacement current density. Note that in clayey materials, while σ' and σ'' both depend on frequency, this dependence is weak as shown and discussed in detail by Vinegar and Waxman (1984) and more recently by Revil (2012, 2013a, b). This dependency will be therefore neglected in the following. The quadrature conductivity of clean sands and sandstones shows a clear frequency peak, but the magnitude of the quadrature conductivity is usually low. The only case of a strong and highly frequency-dependent induced polarization effect is the case of disseminated ores (e.g., sulfides like pyrite and oxides like magnetite). In this case, there is the possibility (still unexplored) to use the seismoelectric method to detect and image ore bodies.

1.3.1 Effective conductivity

The displacement field is related to the electrical field by $\mathbf{D} = \varepsilon \mathbf{E}$ where ε denotes the permittivity or dielectric constant (in F m^{-1}) of the material. We consider a harmonic external electrical field:

$$\mathbf{E} = \mathbf{E}_0 \exp(-i\omega t), \tag{1.85}$$

where f is the frequency in Hz, $\omega = 2\pi f$ denotes the angular frequency (pulsation in rad s^{-1}), and $\mathbf{E}_0$ represents the amplitude of the alternating electrical field. Equation (1.83) can be written as

$$\mathbf{J} = (\sigma^* - \mathrm{i}\omega\varepsilon)\mathbf{E} + \mathbf{J}_S. \tag{1.86}$$

This total current density can be written as an apparent Ohm's law:

$$\mathbf{J} = \sigma_{\mathrm{eff}}{}^* \mathbf{E} + \mathbf{J}_S, \tag{1.87}$$

where $\sigma_{\mathrm{eff}}{}^* = \sigma_{\mathrm{eff}} - i\omega\varepsilon_{\mathrm{eff}}$ is the effective complex conductivity and σ_{eff} and $\varepsilon_{\mathrm{eff}}$ are real positive frequency-dependent scalars (at least in isotropic media) defined by

$$\sigma_{\mathrm{eff}} = \sigma', \tag{1.88}$$

$$\varepsilon_{\mathrm{eff}} = \varepsilon' - \sigma''/\omega. \tag{1.89}$$

Equations (1.88) and (1.89) are a direct consequence of Ampère's law in which the conductivity is considered complex (ion drift is coupled to diffusion), the permittivity is real, and the Maxwell–Wagner polarization and the polarization of the water molecules at few GHz are neglected. The effective properties measured in the laboratory or in the field contain both dielectric and conduction components. It is clear from Equation (1.89) that the effective permittivity is expected to be very strong at low frequencies

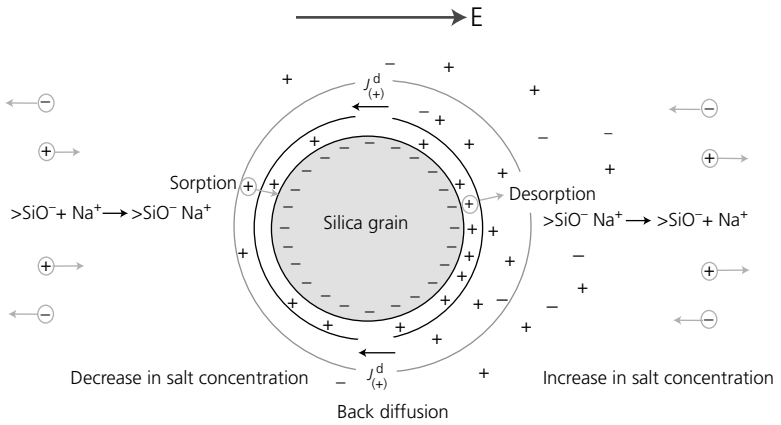

Figure 1.12 The presence of an applied electrical field **E** creates a dipole moment associated with the transfer of the counterions in both the Stern and the diffuse layers around a silica grain. This dipole moment points in the direction that is opposite to the applied field. The charge attached to the mineral framework remains fixed. The movement of the counterions in the Stern layer is mainly tangential along the surface of the grain. However, sorption and desorption of the counterions are in principle possible. Back diffusion of the counterions can occur both in the Stern and diffuse layers, and diffusion of the salt occurs in the pore space. In both cases, the diffusion of the counterions occurs over a distance that is equal to the diameter of the grain.

due to the quadrature conductivity-related term σ''/ω. A discussion of the frequency dependence of σ'' upon the effective permittivity can be found in Revil (2013a, b).

The polarization of the electrical double layer (called the α-polarization in electrochemistry) plays a dominant role at low frequencies through the apparent permittivity of the material (see Figure 1.12). This is in contrast with ideas expressed in the geophysical literature since Poley et al. (1978). In the prior geophysical literature, low-frequency polarization is envisioned to be dominated by the Maxwell–Wagner polarization (also called "space charge" or "interfacial" polarization) due to the discontinuity of the displacement current at the interfaces between the different phases of a porous composite.

1.3.2 Saturated clayey media

Assuming that clayey materials exhibit a fractal or self-affine behavior through a broad range of scales (e.g., Hunt et al., 2012), the inphase and quadrature conductivities are expected to be weakly dependent on frequency as discussed in detail by Vinegar and Waxman (1984) and Revil (2012). This has been shown for a range of frequencies typically used in laboratory measurements (0.1 mHz to 0.1 MHz). Revil (2013a) recently developed a model to describe the complex conductivity of clayey materials using a volume-averaging approach. According to this model, the inphase conductivity σ' (S m^{-1}) is given as a function of the pore water conductivity σ_w (in S m^{-1}) by the following expression:

$$\sigma' = \frac{1}{F}\left\{\sigma_w + \left(\frac{F-1}{F\phi}\right)\rho_S\left[\beta_{(+)}(1-f) + \beta^S_{(+)}f\right]\mathrm{CEC}\right\}, \quad (1.90)$$

where F is the so-called formation factor, ϕ is the porosity, f denotes the fraction of counterions in the Stern layer, ρ_S denotes the mass density of the solid phase (typically 2650 kg m^{-3}), $\beta_{(+)}$ corresponds to the mobility of the counterions in the diffuse layer, and $\beta^S_{(+)}$ denotes the mobility of the counterions in the Stern layer (both in m^2 s^{-1} V^{-1}). The partition coefficient, f, is salinity dependent as discussed in Sections 1.1.1 and 1.1.2. For clay minerals (and for silica as well), the mobility of the counterions in the diffuse layer is equal to the mobility of the same counterions in the bulk pore water (e.g., $\beta_{(+)}(\mathrm{Na}^+, 25°\mathrm{C}) = 5.2 \times 10^{-8}$ m^2 s^{-1} V^{-1}). The mobility of the counterions in the Stern layer is substantially smaller and equal to $\beta^S_{(+)}(25°\mathrm{C}, \mathrm{Na}^+) = 1.5 \times 10^{-10}\mathrm{m}^2\mathrm{s}^{-1}\mathrm{V}^{-1}$ for clay minerals (Revil, 2012, 2013a, b), therefore about 350 times less mobile than in bulk solution. We can rewrite the inphase conductivity equation as

$$\sigma' \approx \frac{1}{F}\sigma_w + \left(\frac{1}{F\phi}\right)\rho_S\left[\beta_{(+)}(1-f) + \beta^S_{(+)}f\right]\mathrm{CEC} \quad (1.91)$$

The surface conductivity corresponds to the last term of Equation (1.91). Equation (1.91) represents the full

saturation version of a more general model. This model implies that the surface conductivity is controlled either by the grain diameter (or from the grain diameter probability distribution as discussed by Revil & Florsch, 2010; see Figure 1.13a) or by the CEC (Figure 1.13b). Surface conductivity could be also expressed as a function of the specific surface area. Indeed, the CEC and the specific surface area are related to each other by Equation (1.34): $Q_0^S = \mathrm{CEC}/S_{sp}$ where Q_0^S, the surface charge density of the counterions, is about 0.32 C m^{-2} for clay minerals. For silica grains, there is a relationship between the mean grain diameter and the surface area or the equivalent CEC of the material. Indeed, the specific surface area S_{sp} was calculated from the median grain diameter, d, using $S_{sp} = 6/(\rho_s d)$ where $\rho_s = 2650$ kg m^{-3} denotes the density of the silica grains. This also yields an equivalent CEC given by $\mathrm{CEC} = 6\ \mathrm{CEC} = 6Q_0^S/(\rho_s d)$ with $Q_0^S = 0.64$ C m^{-2}, and $\rho_s = 2650$ kg m^{-3}. In Figure 1.13b, the surface conductivity data of silica sands and glass beads and clayey media are all along a unique trend. This is consistent with the idea that surface conductivity is dominated by the diffuse layer. Indeed, the mobility of the counterions in the Stern layer is much smaller than the mobility of the counterions in the bulk pore water (see discussion in Revil, 2012, 2013a, b).

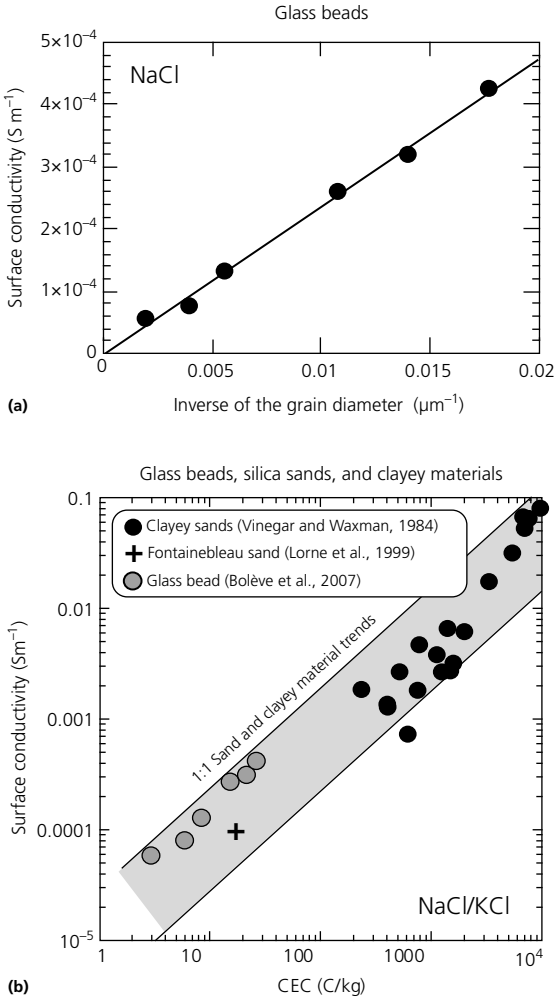

Figure 1.13 Surface conductivity. **a)** For glass beads and silica sands, the surface conductivity is controlled by the size of the grains (Data from Bolève et al., 2007). **b)** All the data for glass beads, silica sands, and shaly sands are on the same trend when plotted as a function of the (total) CEC. This is consistent with a surface conductivity model dominated by the contribution of the diffuse layer (Data from Vinegar & Waxman, 1984 (shaly sands, NaCl); Bolève et al., 2007 (glass beads, NaCl); and Lorne et al., 1999a, b (Fontainebleau sand KCl)).

The quadrature conductivity expression obtained by Revil (2013a) is

$$\sigma'' \approx -\left(\frac{1}{F\phi}\right)\rho_s \beta_{(+)}^S f\,\mathrm{CEC}. \tag{1.92}$$

For the reasons explained previously for the surface conductivity, the quadrature conductivity can be expressed as a function of the specific surface area or as a function of the CEC. At saturation, a comparison between the equation for the quadrature conductivity and experimental data is shown in Figure 1.14 where we used the relationship between the CEC and the specific surface area given by Equation (1.53).

For clayey sands, taking $\beta_{(+)}^S(\mathrm{Na}^+) = 1.5 \times 10^{-10}$ m^{2}s^{-1}V^{-1} at 25°C, $f = 0.90$, $Q_0^S = 0.32$ C m^{-2}, and $\rho_s = 2650$ kg m^{-3}, yields $\sigma'' \approx -cS_{Sp}$ with $c = 7.6 \times 10^{-8}$ S kg m^{-3}. For the clean sands and sandstones, using $\beta_{(+)}(\mathrm{Na}^+) = 5.2 \times 10^{-8}$ m^2 s^{-1} V^{-1}, $f = 0.50$, $Q_0^S = 0.64$ C m^{-2}, and $\rho_s = 2650$ kg m^{-3}, yields $c = 2.9 \times 10^{-5}$ S kg m^{-3}. The difference between the trend for the clean sands and sandstones and the trend for the clayey materials illustrates how different are the mobilities of the counterions in the Stern layer of silica and clays. In Figure 1.15, we plot directly the quadrature conductivity as a function of the CEC for shaly sands. In Figure 1.16, we plot the quadrature conductivity of sands as a function of the mean grain diameter. Using the transform given previously between the mean grain diameter and the CEC, we plot in Figure 1.17 the quadrature conductivity as a function

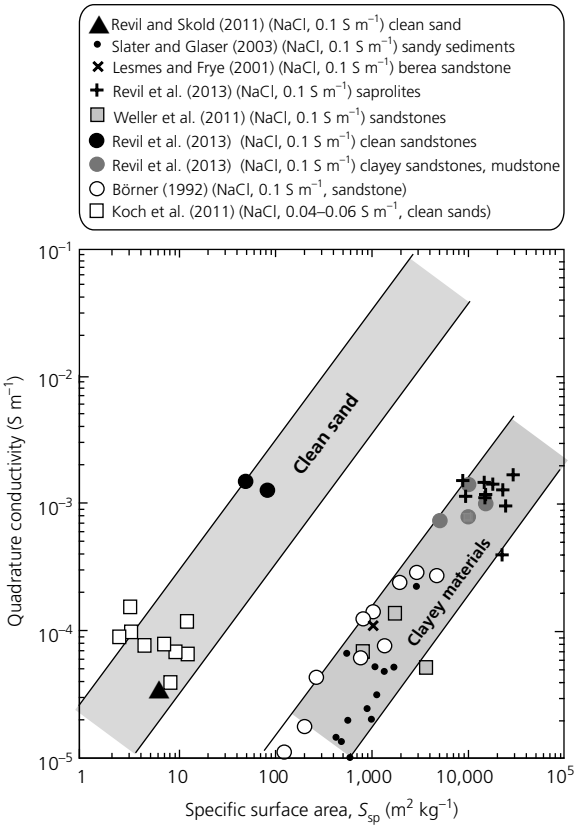

Figure 1.14 Influence of the specific surface area S_{Sp} upon the quadrature conductivity, which characterizes charge accumulation (polarization) at low frequencies. The trend determined for the clean sands and the clayey materials are from the model developed by Revil (2012) at 0.1 S m^{-1} NaCl. The measurements are reported at 10 Hz. Data from Revil and Skold (2011), Koch et al. (2011), Slater and Glaser (2003), Lesmes and Frye (2001), Revil et al. (2013), and Börner (1992).

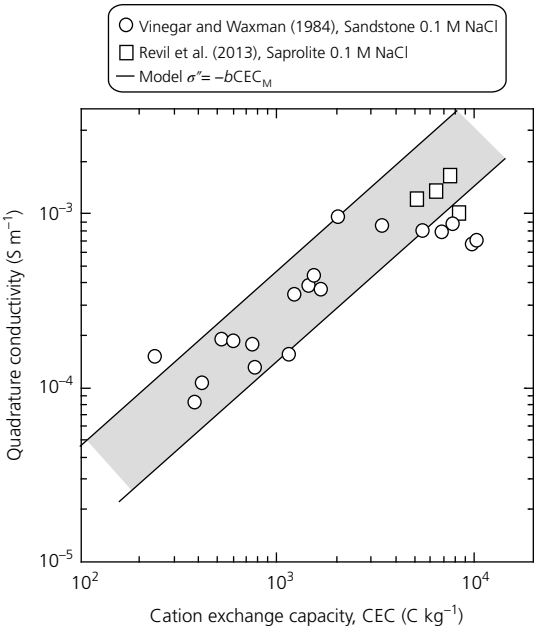

Figure 1.15 Influence of the cation exchange capacity (CEC) upon the quadrature conductivity of clayey materials. The trend is determined for the clayey materials from the model developed by Revil (2012, 2013) at 0.1 mol l^{-1} NaCl (about 1 S m^{-1}). The measurements are from Vinegar and Waxman (1984) (shaly sands) and Revil et al. (2013) (saprolites). Note that the slope of this trend is salinity dependent.

of the CEC. The data are corrected for the dependence of the partition coefficient f with the salinity using the approach developed by Revil and Skold (2011). These data exhibit two distinct trends indicating that the mobility of the counterions in the Stern layer of silica is equal to the mobility of the same ions in the bulk pore water, while the mobility of the counterions at the surface of clays is much smaller than in the bulk pore water. For clayey materials, it is also clear that the surface conductivity can be directly related to the quadrature conductivity as discussed by Revil (2013a, b).

The following dimensionless number can be defined as $R \equiv -\sigma''/\sigma_S \geq 0$, which corresponds therefore to the ratio of quadrature, σ'', to surface conductivity, σ_s. With this definition, the complex conductivity of a partially saturated porous siliciclastic sediment can be written as

$$\sigma^* = \frac{1}{F}\sigma_w[1 + \mathrm{Du}(1 - i\mathrm{R})], \tag{1.93}$$

$$\mathrm{Du} = \frac{F\sigma_S}{\sigma_w}. \tag{1.94}$$

As briefly discussed by Revil and Skold (2011) and Revil (2012, 2013a), the ratio R can be related to the partition coefficient f. In the present case, we obtain

$$R = \frac{\beta^S_{(+)} f}{\left[\beta_{(+)}(1-f) + \beta^S_{(+)} f\right]}, \tag{1.95}$$

$$R(\mathrm{clay}) \approx \frac{\beta^S_{(+)} f}{\beta_{(+)}(1-f)}, \tag{1.96}$$

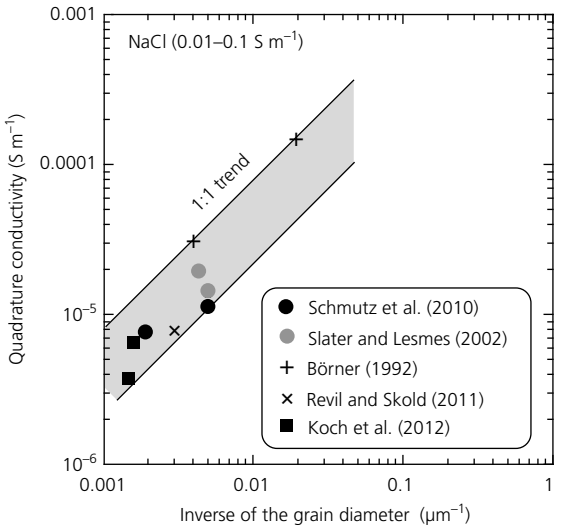

Figure 1.16 Influence of the mean grain diameter upon the quadrature conductivity of sands. Pore water conductivity in the range 0.01–0.1 S m^{-1} NaCl. The measurements are from Schmutz et al. (2010), Slater and Lesmes (2002), Börner (1992), Revil and Skold (2011), and Koch et al. (2012). The quadrature conductivities in this figure are reported at the relaxation peak.

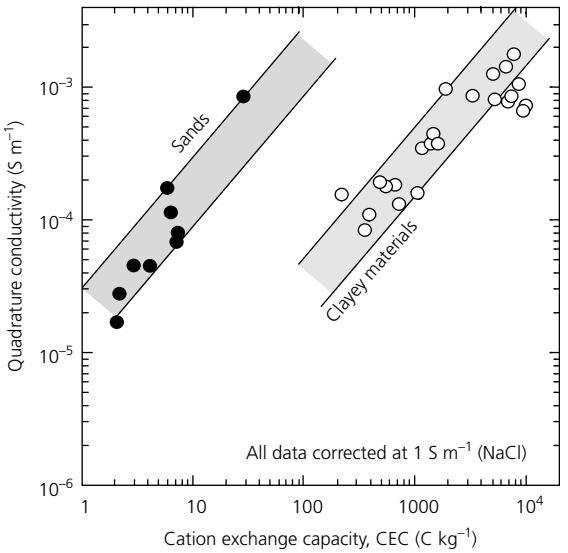

Figure 1.17 Trends for the quadrature conductivity versus CEC for sands and clayey materials. All the experimental data are corrected for salinity to bring them to a pore water conductivity of 1 S m^{-1} (NaCl) using the salinity dependence of f the fraction of counterions in the Stern layer. The two different trends between the silica sands and the clayey materials are an indication that the mobility of the counterions in the Stern layer is much smaller for clay minerals than for silica. This plot shows how difficult it is to extract the petrophysical properties of formations from the quadrature conductivity alone. Indeed, formations with very different permeabilities and lithologies can have the same quadrature conductivity.

$$R(\text{sand}) \approx f. \tag{1.97}$$

We can analyze the value of R for sands and clays. For sands, taking $\beta^{S}_{(+)}(Na^+, 25°C) = \beta_{(+)}(Na^+, 25°C) = 5.2 \times 10^{-8}\,m^2\,s^{-1}\,V^{-1}$, $f = 0.50$ (f depends actually on pH and salinity; see Figure 1.6), we have $R \approx 0.50$. In the case of clay minerals, taking $\beta^{S}_{(+)}(Na^+, 25°C) = 1.5 \times 10^{-10}$ $m^2\,s^{-1}\,V^{-1}$ and $\beta_{(+)}(Na^+,\ 25°C) = 5.2 \times 10^{-8}\,m^2\,s^{-1}\,V^{-1}$, $f = 0.90$, yields $R = 0.0260$. In both cases, the results are consistent with the experimental results displayed in Figures 1.13 and 1.17.

1.4 Principles of the seismoelectric method

Now that the electrical double layer has been described and the direct consequences of the existence of this electrical double layer discussed, we need to introduce the key concepts behind the seismoelectric method.

1.4.1 Main ideas

The electroseismic (electric to seismic) and seismoelectric (seismic to electric) phenomena correspond to two symmetric couplings existing between EM and seismic disturbances in a porous material (Frenkel, 1944; Pride, 1994). The electroseismic effects correspond to the generation of seismic waves when a porous material is submitted to a harmonic electrical field or electrical current. The seismoelectric effects correspond to the generation of electrical (possibly EM) disturbances when a porous material is submitted to the passage of seismic waves. The electroseismic and seismoelectric couplings are both controlled by the relative displacement between the charged solid phase (with the Stern layer attached to it) and the pore water (with its diffuse layer and consequently an excess of electrical charges per unit pore volume).

Figure 1.18 sketches the general idea underlying the seismoelectric theory. We consider porous media in which seismic waves propagate. The description of the propagation of the seismic waves depends on the

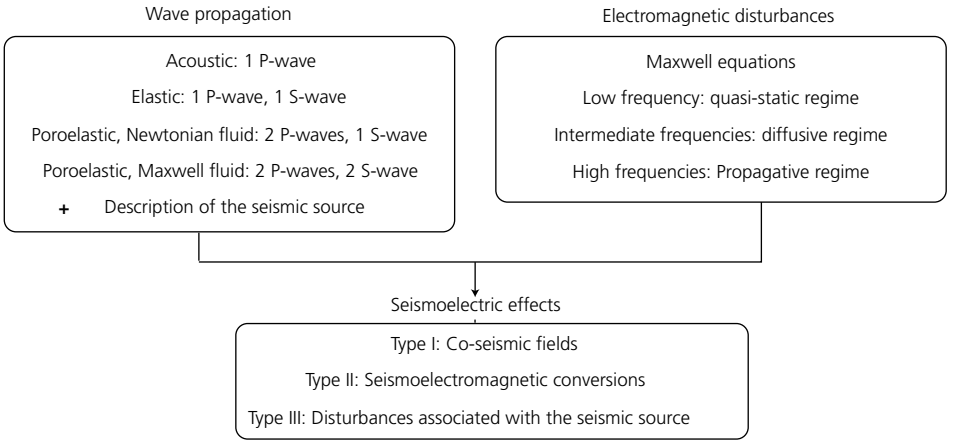

Figure 1.18 General concept of seismoelectric disturbances. Seismoelectricity combined the propagation of seismic (compressional and rotational) waves in porous materials. These porous materials are considered to be composites with phases carrying a net charge density (the material as a whole is neutral). The mechanical equations are coupled to the Maxwell equations through a source current density and a source of momentum. Three types of seismoelectric disturbances can be observed: Type I corresponds to the electromagnetic fields traveling with the seismic wave itself (coseismic fields). Type II corresponds to the electromagnetic disturbances associated with the passage of a seismic wave through a macroscopic heterogeneity (seismoelectric conversion). Type III corresponds to the electromagnetic fields associated with a seismic source. S corresponds to shear wave, while P corresponds to compressional (pressure) wave (the letters P and S are also used in terms of arrival time: primary and secondary waves).

rheology of the material and its dispersive properties. In this book, we will consider various rheological behaviors leading to different types and numbers of waves. For instance, the acoustic theory applied to porous media can only be used to describe, in an approximate way, the propagation of compressional (*P* for pressure) waves in porous media. A refinement of this theory is to consider the elastic case. The elastic case implies that two types of seismic waves are generated: pressure (P-)waves and shear (S-)waves. That said, porous media are composite of mineral and fluids, so a more complicated theory exists to describe more accurately seismic wave propagation in porous media. This corresponds to the theory of poroelasticity.

A macroscopic linear poroelastic theory of wave propagation has been first proposed by Biot (1962a, b). Microscopic theories of poroelasticity have been also proposed by various authors, but they will not be reviewed in this book. The poroelastic theory proposed by Biot leads to two P-waves (a slow P-wave and a fast one) and one S-wave. Revil and Jardani (2010) generalized the Biot–Frenkel theory to the case where the fluid can sustain shear stresses. This theory will be developed in Chapter 2. It yields to two P-wave and two S-wave propagation models and provides a symmetric theory, while the biotheory is asymmetric in its equations as the fluid does not sustain shear stresses. Whatever the theory used, the propagation of the seismic waves through a porous material is responsible for a movement of the water with respect to the solid phase. In the presence of an electrical double layer, this relative displacement is the source for an electrical current density. This current density acts a source term in the Maxwell equations generating EM disturbances. These EM disturbances are described by the Maxwell equations, which takes the general form of the coupled telegraph equations for the electrical and magnetic fields (these partial differential equations contain propagative and diffusive terms). If we consider low-frequency seismic waves, the time-dependent terms can be dropped from the telegraphist's equations, and we end up with Poisson equations for the electrical and magnetic fields. Three types of EM disturbances can be generated: Type I corresponds to the EM fields traveling with the seismic waves themselves. These are generally called the coseismic fields and can only be observed in the volume directly affected by the propagation of the seismic waves. Type II corresponds to EM effects associated with the passage of seismic waves through a macroscopic heterogeneity (seismoelectric conversion). They can be remotely observed, away from

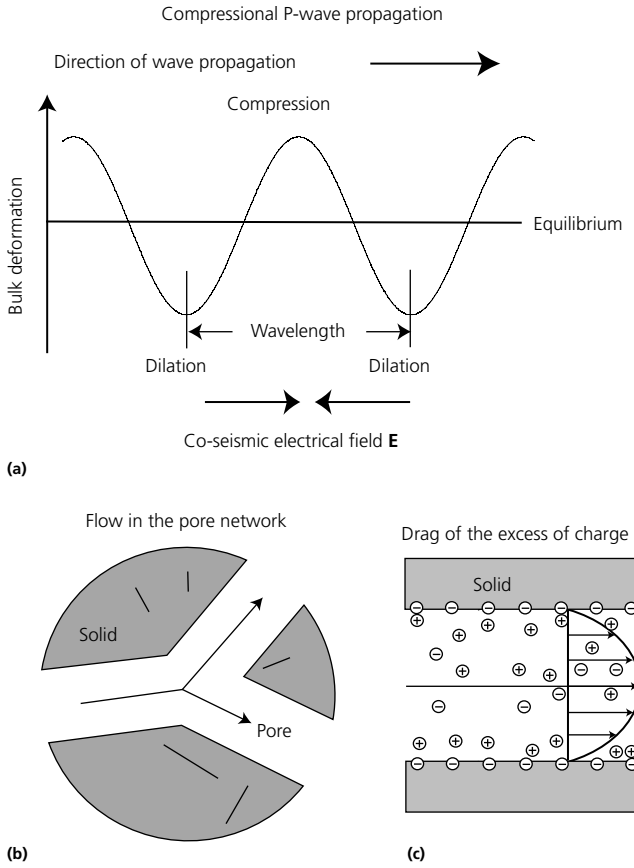

Figure 1.19 The coseismic electrical field and the coseismic (streaming) electrical current. **a)** The propagation of a compressional (pressure or P-)wave through a porous material generates areas of compression and dilation (expansion). **b)** In response to the change in the mechanical stresses, the pore water flows from the compressed regions to the dilated regions. **c)** The flow generates a streaming current density that is locally counterbalanced by the conduction current density creating, locally, an electrical field **E** of electrokinetic nature.

the interface. Finally, Type III corresponds to the EM fields associated with the seismic source itself.

We first describe Type I and II seismoelectric effects. When seismic waves propagate in a linear poroelastic porous material, two types of electrical disturbances are observed (Figures 1.19 and 1.20). The propagation of compressional P-waves generates an electrical source current associated with the displacement of the electrical diffuse layer in a Lagrangian framework attached to the solid phase (Figure 1.19). Inside a wavelength of a compressional wave, there are areas of dilation and compression (Figure 1.19a). These dilations and compressions of the solid skeleton are responsible for the flow of the pore water from the compressed regions to the regions where expansion occurs (Figure 1.19b). As the result of the flow of the pore water, there is the advective drag of a fraction of the excess of charge of the pore water. This advective drag is responsible for the streaming current density. Shear (S-)waves do not create coseismic electrical field. These coseismic electrical signals travel at the same speed as the seismic waves (Pride, 1994). The amplitudes of the coseismic EM signals are controlled by the properties of the porous material (the formation factor) and by the properties of the pore fluid/solid interface (the zeta potential in the theory of Pride (1994), the excess charge per unit pore volume in the formulation used in this book).

In addition to the coseismic signals, another phenomenon occurs when a seismic wave moves through a sharp interface characterized by a change in the textural properties or a change in salinity or clay content or mineralogy (Figure 1.20). In this situation, a fraction of the mechanical energy is converted into EM energy, and a dipolar EM excitation is produced at the interface. The resulting EM disturbances diffuse very quickly away through the interface and can be recorded, nearly instantaneously, by electrodes or antennas located at the ground surface, in boreholes, or at the seafloor, for instance. In the seismoelectric method, we are mostly

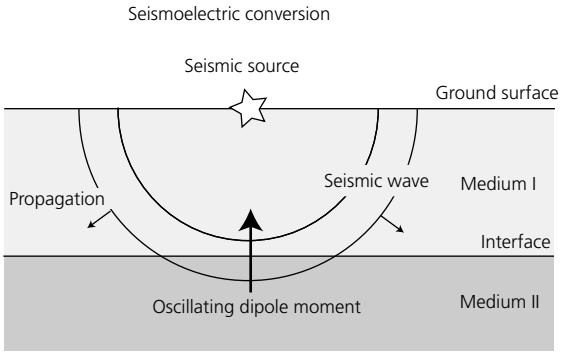

Figure 1.20 The seismoelectric conversion (called sometimes the interface response) results from the generation of an unbalanced source current density at an interface during the passage of a seismic wave. The divergence of the source current density at the interface is mathematically similar to an oscillating dipole moment generated at the interface in the first Fresnel zone. The star represents the seismic source.

interested in the information content associated with these conversions. However, the magnitude of these conversions decreases very quickly with the distance from the interface. In Chapters 2 and 3, we will provide a general theory of the coseismic field and seismoelectric conversion in saturated and partially saturated cases, respectively, and we provide in Section 1.4.2 a simple modeling approach based on the acoustic approximation.

A third effect corresponds to the EM fields generated directly by a seismic source. We will see that these EM fields (especially the electric component) can be combined with the radiated seismic fields and used to localize the seismic source and characterized the moment tensor of the source. These effects will be fully explored in Chapter 5.

1.4.2 Simple modeling with the acoustic approximation

1.4.2.1 The acoustic approximation in a fluid

We consider a fluid with its viscous effects considered to be negligible in the momentum conservation equation. The propagation of a seismic wave in this fluid can be described in terms of a pressure perturbation $p(\mathbf{r}, t)$ (true pressure minus the equilibrium pressure) or in terms of a fluid displacement $\mathbf{u}(\mathbf{r}, t)$. The volume strain θ is related to the displacement by

$$\theta = \frac{\Delta V}{V} = \nabla \cdot \mathbf{u}, \tag{1.98}$$

where $\Delta V/V$ represents a relative variation of volume during the passage of the seismic wave. The compressibility of the fluid is defined, in isothermal conditions, as

$$\beta_f = \frac{1}{K_f} = -\frac{1}{V}\left(\frac{\partial V}{\partial p}\right)_T, \tag{1.99}$$

and K_f denotes the bulk modulus (in Pa). Therefore, the pressure perturbation is related to the displacement by

$$p = -K_f\theta = -K_f \nabla \cdot \mathbf{u}. \tag{1.100}$$

Equation (1.100) corresponds to Hooke's law for a fluid and is valid for small deformation ($\theta \ll 1$). Equation (1.100) corresponds to a constitutive equation. To get the field equation for the pressure perturbation p, we need to combine Equation (1.100) with a conservation equation. Newton's law provides the required conservation equation for the momentum

$$-\nabla p = \rho_f \ddot{\mathbf{u}}, \tag{1.101}$$

where ρ_f denotes the density of the fluid (assumed to be constant) and $\ddot{\mathbf{u}}$ corresponds to the acceleration of the material. As we need to express the divergence of the fluid displacement in terms of fluid pressure, we want to take the divergence of Equation (1.101). This yields

$$-\nabla^2 p = \rho_f \frac{\partial^2}{\partial t^2}(\nabla \cdot \mathbf{u}), \tag{1.102}$$

$$\nabla^2 p = \frac{\rho_f}{K_f}\frac{\partial^2 p}{\partial t^2}, \tag{1.103}$$

$$\nabla^2 p - \frac{1}{c_f^2}\frac{\partial^2 p}{\partial t^2} = 0 \tag{1.104}$$

where

$$c_f = \left(\frac{K_f}{\rho_f}\right)^{1/2}. \tag{1.105}$$

Equation (1.104) corresponds to the wave equation for the fluid pressure with the velocity given by Equation (1.105). If we wish to determine the displacement of the fluid, we can, for instance, consider a wave with a sinusoidal time dependence given by

$$p(\mathbf{r}, t) = p_\omega(\mathbf{r}) exp(-i\omega t), \tag{1.106}$$

where i denotes the pure imaginary number and ω is the angular frequency. Inserting Equation (1.106) into Equation (1.104) shows that the amplitudes obey the scalar Helmholtz equation:

$$\nabla^2 p_\omega(\mathbf{r}) + \frac{\omega^2}{c_f^2} p_\omega(\mathbf{r}) = 0. \tag{1.107}$$

If we consider Newton's law, Equation (1.101), we obtain the following equation for the displacement of the fluid:

$$\mathbf{u}(\mathbf{r}, t) = -\frac{1}{\rho_f \omega^2} \nabla p_\omega(\mathbf{r}) exp(-i\omega t). \tag{1.108}$$

Because the curl of a gradient is always equal to zero, we have the property

$$\nabla \times \mathbf{u}(\mathbf{r}, t) = 0. \tag{1.109}$$

The displacement is irrotational, which means that the pressure wave is purely longitudinal and corresponds to a P-wave with a seismic velocity given by Equation (1.105).

1.4.2.2 Extension to porous media

Usually, the seismoelectric problem is formulated in terms of a coupling between the Maxwell equations and the Biot–Frenkel theory (e.g., Pride, 1994; Revil & Jardani, 2010), and the Biot–Frenkel theory will be discussed in Chapter 2. In the present section, we adapt the acoustic wave developed in the previous section to a porous body, and we simplify the seismoelectric theory to make it compatible with this acoustic approximation. We need an acoustic approximation solving now for the macroscopic pressure perturbation P of a porous material containing a fluid that cannot support shear stress (for instance, water). This formulation is obtained by adapting Equation (1.104) to a porous material:

$$\frac{\partial^2 P}{\partial t^2} - K \nabla \cdot \left(\frac{1}{\rho} \nabla P \right) = f(\mathbf{r}, t), \tag{1.110}$$

where P denotes the confining pressure (in Pa), ρ is the mass density of the material (in kg m^{-3}), K is the bulk modulus of the porous material (in Pa), and $f(\mathbf{r}, t)$ denotes the source function (seismic source) at position $\mathbf{r}$ and time t. The acoustic pressure corresponds to the hydrostatic part of the stress tensor $\mathbf{T}$:

$$P = -\frac{1}{3} \text{Trace} \mathbf{T}. \tag{1.111}$$

Still, Equation (1.111) is not good enough to be compatible with the velocity of the P-wave in a porous material. First, the bulk modulus that should be considered is generally the undrained bulk modulus (the fluid in the pores resists to the deformation). The modulus K_u (in Pa) is defined by

$$K_u = \frac{K_f(K_s - K) + \phi K(K_s - K_f)}{K_f(1 - \phi - K/K_s) + \phi K_s}. \tag{1.112}$$

In addition, the porous material, at the opposite of a viscous fluid, can sustain shear stresses. This means that Equation (1.110) needs to be replaced by

$$\frac{\partial^2 P}{\partial t^2} - \left(K_u + \frac{4}{3} G \right) \nabla \cdot \left(\frac{1}{\rho} \nabla P \right) = f(\mathbf{r}, t), \tag{1.113}$$

where G is described as the shear modulus of the skeleton (frame) of the porous material (the reason for the term $K_u + (4/3)G$ can be obtained from elastic theory). Equation (1.113) can be used to solve the poroacoustic problem for the P-wave propagation in a porous material. Assuming that the viscous coupling between the pore water and the solid phase can be neglected, the velocity of the P-waves is approximated by (Gassmann, 1951)

$$c_p = \left(\frac{K_u + \frac{4}{3} G}{\rho} \right)^{\frac{1}{2}}. \tag{1.114}$$

Now, we need to describe how the macroscopic perturbation P on the elastic skeleton affects the pore fluid pressure p, at least in an approximate way. In the undrained regime of poroelasticity, the pressure, P, is related to the so-called undrained pore fluid pressure p by (see Section 1.5.3)

$$p = BP, \tag{1.115}$$

where $0 \leq B \leq 1$ is called the Skempton coefficient (see Section 1.5). It is given by

$$B = \frac{1 - K/K_u}{1 - K/K_S}, \tag{1.116}$$

where K is the bulk modulus (in Pa), K_u is the undrained bulk modulus (in Pa), and K_S is the bulk modulus of the

solid phase (in Pa). The passage of the wave generates a confining pressure fluctuation, P, on a representative elementary volume of the rock, more precisely on the elastic skeleton. This change in confining pressure generates in turn a change in the pore fluid pressure and therefore the flow of the pore water according to Darcy's law. Moreover, the flow of pore water relative to the solid phase generates a source current density given by

$$\mathbf{J}_S = \hat{Q}_V^0 \dot{\mathbf{w}} = -\frac{\hat{Q}_V^0 k_0}{\eta_f} \nabla p, \tag{1.117}$$

where $\dot{\mathbf{w}}$ denotes the Darcy velocity discussed in Section 1.2. In getting Equation (1.117), we have neglected the inertial terms, and therefore, this equation considers only low-frequency disturbances (below 1 kHz).

1.4.3 Numerical example of the coseismic and seismoelectric conversions

We use now the acoustic approximation, implemented in the finite-element package COMSOL Multiphysics, to describe the effects of coseismic field and seismoelectric conversion. We start with the coseismic field associated with the traveling of a compressional pressure (P-)wave in a homogeneous material. Figures 1.21, 1.22, and 1.23 show three snapshots showing the propagation of such a wave between a seismic source and a geophone collocated with an electrode (the reference for the electrical potential at the electrode is taken to infinity). We see an electrical signal at the position of the electrode only when the seismic wave arrives at this location. Therefore, the coseismic electrical field is only localized in the spatial support of the seismic wave.

Figure 1.24 shows a snapshot of the electrical potential distribution when a seismic wave hits an interface between two media of different mechanical and electrical properties. In this example, the two layers are only characterized by a difference in electrical conductivity. The seismoelectric conversion at the interface is similar to the one that would be generated by a dipole distribution located along the interface in the first Fresnel zone of then seismic wave. The concept of Fresnel zone will be discussed further in Chapter 4.

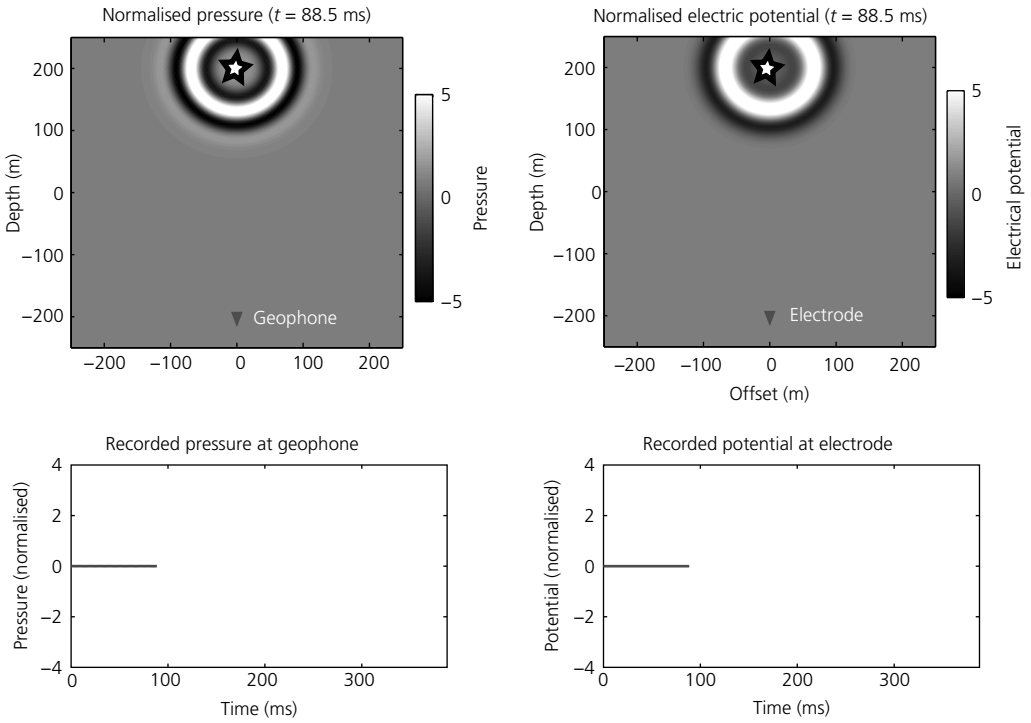

Figure 1.21 Synthetic example computed with the acoustic approximation to demonstrate the effect of the coseismic electrical field. A seismic source generates a pressure wave in a homogeneous material. We see here the normalized pressure (left panel) and the normalized electrical potential (right panel) at time 88.5 ms. The star represents the seismic source. (*See insert for color representation of the figure*.)

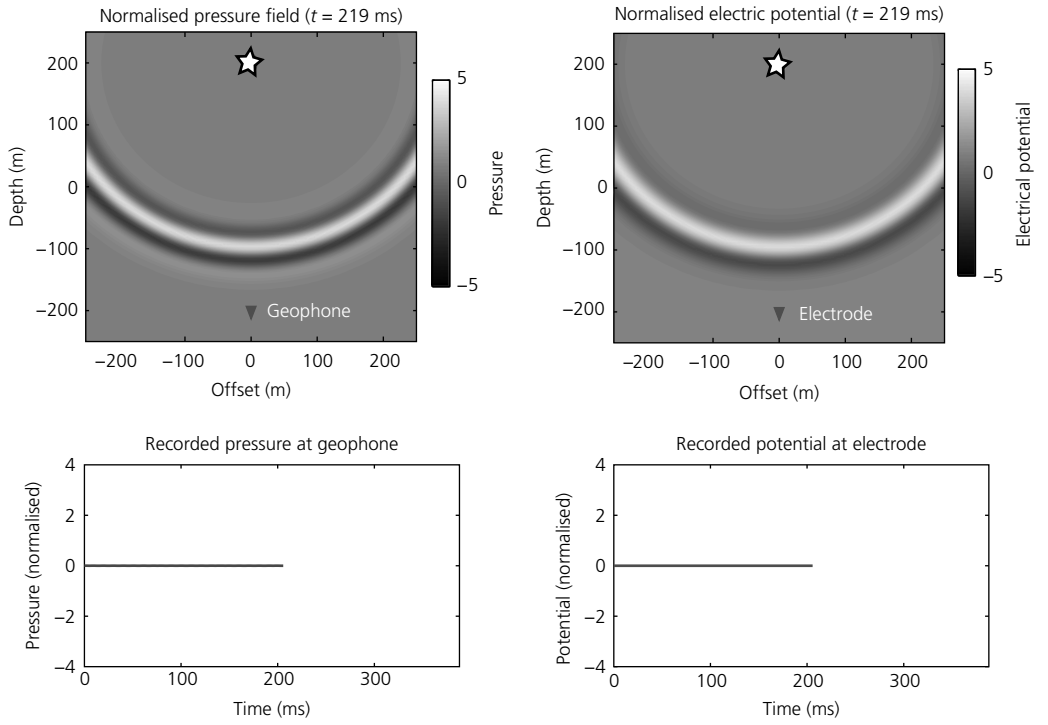

Figure 1.22 Same as Figure 1.18 for time 219.0 ms. The traveling P-wave is located in between the source and the position of the recording geophone located with an electrode (reference electrode to infinity). We see no disturbances at the position of the geophone and electrode. (*See insert for color representation of the figure*.)

1.5 Elements of poroelasticity

In this section, we provide some of the basic tools required to understand static and dynamic poroelasticity. These elements will be used further in Chapter 2 to establish some general models for the seismoelectric theory.

1.5.1 The effective stress law

We consider a porous material with a connected porosity and a solid frame (the skeleton) that behaves elastically. The material is homogeneous at the scale of the representative elementary volume and monomineralic. The stress tensor applied to the porous material is written as **T**. The component of the stress tensor corresponds to T_{ij}, which represents the force per unit surface area imposed from outside in the ith-direction along a surface with normal in the jth-direction (Figure 1.25). The strain (deformation) tensor is defined by

$$\varepsilon_{ij} = \frac{1}{2}\left(\frac{\partial u_i}{\partial x_j} + \frac{\partial u_j}{\partial x_i}\right), \tag{1.118}$$

$$\varepsilon_{ij} = \frac{1}{2}\left(u_{i,j} + u_{j,i}\right), \tag{1.119}$$

where we are using the engineering notations and where the vector **u** refers to the displacement of the solid phase. The (small) change in volume of the material is described as

$$\varepsilon_{kk} = \mathrm{Tr}\left(\varepsilon_{ij}\right) = \nabla\cdot\mathbf{u} = \frac{\delta V}{V}, \tag{1.120}$$

where Tr refers to the trace of the tensor (the sum of the diagonal elements) and $\delta V/V$ denotes a volume element increment. In Equation (1.120), we have used Einstein (summation) convention on repeated indices (Einstein, 1916). This convention implies summation over a set of repeated indices in an equation with the goal to

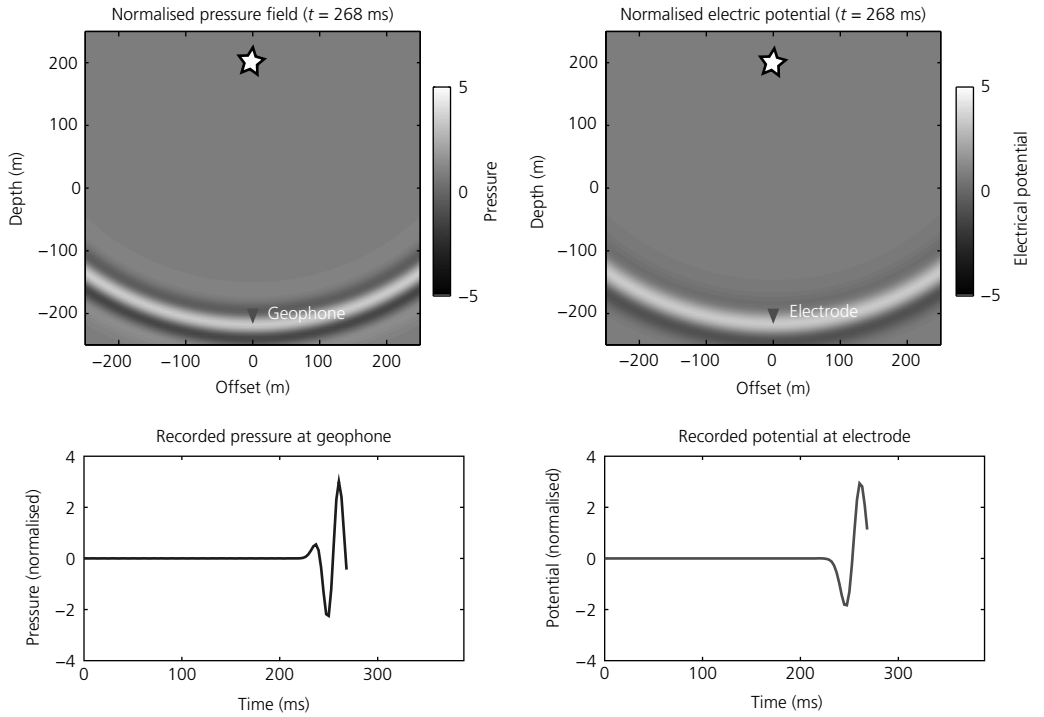

Figure 1.23 Same as Figure 1.18 for time 268.0 ms. The traveling (P-wave) seismic disturbance has reached ith an electrode (reference electrode to infinity). The geophone and the electrode record a pressure and an associated electrical disturbance. The electrical field corresponding to the electrical disturbance is called the coseismic field. (*See insert for color representation of the figure*.)

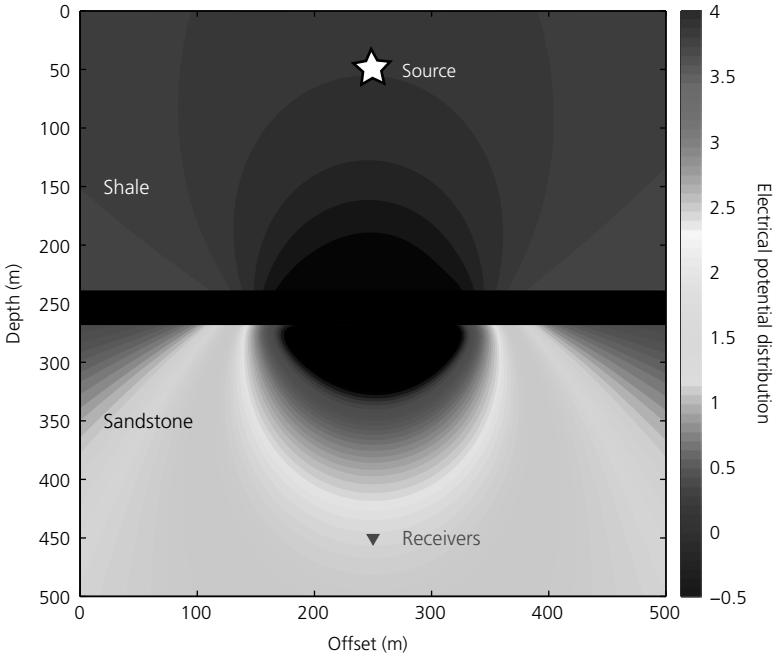

Figure 1.24 Snaphot of the seismoelectrical disturbance (seismoelectric conversion) generated at an interface between two media of different electrical conductivities (here a conductive shale and a less conductive sandstone) during the passage of a seismic P-wave. The star represents the seismic source. The radiation occurs in the first Fresnel zone of the seismic wave. (*See insert for color representation of the figure*.)

achieve notational brevity. The strain tensor is related to its components by

$$\boldsymbol{\varepsilon} = \varepsilon_{ij}\mathbf{x}_i \otimes \mathbf{x}_j, \tag{1.121}$$

where $\mathbf{x}_i$ (i = 1, 2, 3) denote the basis vectors of the Cartesian framework of reference ($\mathbf{x}_i \cdot \mathbf{x}_j = \delta_{ij}$ where δ_{ij} denotes the Kronecker delta) and $\mathbf{a}\otimes\mathbf{b}$ represents the tensorial product between vectors $\mathbf{a}$ and $\mathbf{b}$.

We first consider two states, E1 and E2, that will be combined soon to determine the effective pressure in a porous material. In state E1, we apply a confining pressure P, and we consider no change in the fluid pressure p =0. In this case, the bulk deformation is given by

$$\varepsilon_{kk}(P,0) \equiv \nabla\cdot\mathbf{u}(P,0) = -\frac{P}{K}, \tag{1.122}$$

where the drained bulk modulus of the porous material is defined by

$$\frac{1}{K} = -\frac{1}{V}\left(\frac{\partial V}{\partial P}\right)_{p=0,T} \tag{1.123}$$

and T denotes temperature. In state E2, we apply a confining stress P, and we imposed a fluid pressure equal to the confining stress $p = P$. In this second state, the deformation of the material is controlled by the stiffness of the solid phase (not by the stiffness of the skeleton). Therefore, we have

$$\varepsilon_{kk}(P=p,p) \equiv \nabla\cdot\mathbf{u}(P=p,p) = -\frac{P}{K_S}, \tag{1.124}$$

where K_S, the drained bulk modulus of the solid phase (e.g., silica), is defined by

$$\frac{1}{K_S} = -\frac{1}{V}\left(\frac{\partial V}{\partial P}\right)_{p=P,T}. \tag{1.125}$$

Now, we can describe the general bulk deformation of a porous material in state E as the linear superposition of the two states E1 and E2 as shown in Figure 1.26. This can be written as

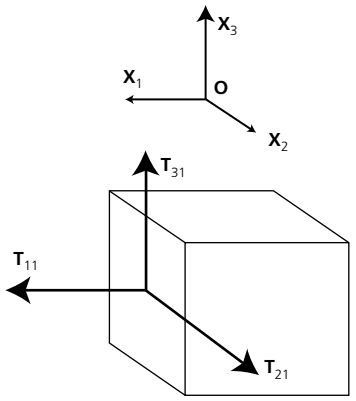

Figure 1.25 Definition of the stress tensor components on a cube of an elastic material. Each component defines a force on one of the face of the cube in a certain direction. These forces are imposed from the external world.

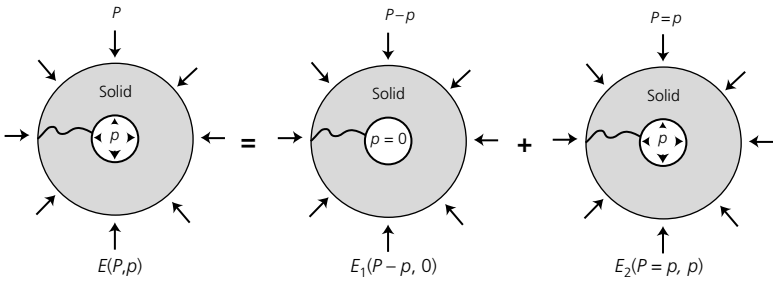

Figure 1.26 Application of the superposition principle used to determine the effective pressure law in a linear poroelastic material. The porous material is composed of a solid phase with an interconnected pore space, which is also connected to the external world. In the general case, we impose a confining pressure P to the porous material, and there is an internal pressure corresponding to the pore fluid pressure p. The general case can be considered as the superposition of two states E1 and E2. In the first state, we apply a confining pressure $P - p$, and therefore is no internal pressure in the pores. In state E2, we apply a confining pressure that is equal to the fluid pressure.

$$E(P,p) = E_1(P-p,0) + E_2(P=p,p). \tag{1.126}$$

Equation (1.124) can be written in terms of bulk deformation as

$$\varepsilon_{kk}(P,p) = \varepsilon_{kk}(P-p,0) + \varepsilon_{kk}(P=p,p), \tag{1.127}$$

$$\varepsilon_{kk}(P,p) = -\frac{1}{K}(P-p) - \frac{1}{K_S}p. \tag{1.128}$$

The bulk deformation can be written in terms of an effective pressure P^* as

$$\varepsilon_{kk}(P,p) = -\frac{1}{K}P^*, \tag{1.129}$$

$$P^* = P - \alpha p, \tag{1.130}$$

$$\alpha = 1 - \frac{K}{K_S}. \tag{1.131}$$

The coefficient α is called the effective stress coefficient or Biot coefficient. Equation (1.129) means that from the standpoint of the bulk deformation, having a confining pressure P and an internal pore fluid pressure p is equivalent of having a confining pressure P^* and no fluid pressure. We can proceed now to a complete analysis of the Biot coefficient α. We have $K_S \geq K$ and therefore $\alpha \geq 0$. If $K_S \gg K$ (for instance, at high porosity, the compressibility of the skeleton is high), we have $\alpha = 1$. In this last case, the effective pressure is equal to the differential pressure $P-p$. This situation is known as the Terzaghi effective stress principle (Terzaghi, 1943) and was developed initially for porous soils. In the case where the porosity is equal to zero, we have $K = K_S$, and therefore, $\alpha = 0$, which is consistent with the idea that at very low porosity (e.g., for crystalline rocks), the fluid pressure will play no role. A typical value of the Biot coefficient for a sandstone is 0.8.

1.5.2 Hooke's law in poroelastic media

In a linear poroelastic material, the constitutive Hooke's law is written as

$$T_{ij} = \left(K - \frac{2}{3}G\right)\varepsilon_{kk}\delta_{ij} + 2G\varepsilon_{ij} - \alpha p\delta_{ij}, \tag{1.132}$$

where δ_{ij} is the Kronecker delta defined by

$$\delta_{ij} = \begin{cases} 0 & \text{if } i \neq j \\ 1 & \text{if } i = j \end{cases} \tag{1.133}$$

and G denotes the shear modulus of the material, which is equal to the shear modulus of the skeleton (as long as the fluids do not sustain shear stresses). The two first terms of the right-hand side of Equation (1.132) correspond to the classical Hooke's law in elastic media, and the last term corresponds to the effect of the pore fluid pressure. We are going to demonstrate that this equation is consistent with the effective pressure law determined in Section 1.5.1.

Taking the nondiagonal components of Equation (1.132) yields

$$T_{ij}(i \neq j) = 2G\varepsilon_{ij}, \tag{1.134}$$

which corresponds to pure shear. We look now for Hooke's law for the bulk deformation. We have

$$T_{kk} \equiv \mathrm{Tr}(\mathbf{T}), \tag{1.135}$$

$$T_{kk} \equiv 3(K\varepsilon_{kk} - \alpha p), \tag{1.136}$$

where $\mathrm{Tr}(\cdot)$ denotes the trace of the matrix corresponding to the tensor (sum of the diagonal elements). The confining pressure is related to the bulk stress by

$$P \equiv -\frac{1}{3}T_{kk} = -K\varepsilon_{kk} - \alpha p, \tag{1.137}$$

and therefore, we can check the property

$$\varepsilon_{kk} = -\frac{1}{K}(P - \alpha p) = -\frac{1}{K}P^*, \tag{1.138}$$

which is consistent with Equation (1.129).

1.5.3 Drained versus undrained regimes

In the drained regime, the fluid is free to move in and out of a representative elementary volume that is undergoing deformation, and doing so, it dissipates energy. The fluid pressure can be considered as constant, and the mass of fluid per unit volume of rock is variable. In the undrained regime, the fluid cannot (or has no time to) move in/out with respect to the representative elementary volume. In this case, the fluid resists to the deformation. The drained and the undrained bulk moduli are defined by

$$\frac{1}{K} = -\frac{1}{V}\left(\frac{\partial V}{\partial P}\right)_{p,T}, \tag{1.139}$$

$$\frac{1}{K_u} = -\frac{1}{V}\left(\frac{\partial V}{\partial P}\right)_{m,T}. \tag{1.140}$$

Obviously, it is harder to deform a rock if some fluid (for instance, water) is resisting the deformation. Consequently, we have the following property: $K_S \geq K_u \geq K$. The undrained regime is defined by replacing the porous material by an equivalent elastic material with a bulk modulus K_u (the shear modulus remains unchanged). In the undrained regime, Hooke's law is therefore given by

$$T_{ij} = \left(K_u - \frac{2}{3}G\right)\varepsilon_{kk}\delta_{ij} + 2G\varepsilon_{ij}. \tag{1.141}$$

We can look for the bulk deformation of the material in the undrained regime (the pure shear components are unchanged with respect to the drained case). This yields

$$T_{kk} = 3K_u\varepsilon_{kk}, \tag{1.142}$$

and therefore,

$$\varepsilon_{kk} = \frac{1}{3K_u}T_{kk} = -\frac{P}{K_u}. \tag{1.143}$$

What about the fluid pressure in the undrained case? We can still apply the complete form of Hooke's law by writing that the fluid pressure is equal to the undrained fluid pressure. The effective stress law yields

$$\varepsilon_{kk}(P, p_u) = -\frac{1}{K}(P - \alpha p_u). \tag{1.144}$$

Equating Equations (1.143) and (1.144) yields

$$\frac{P}{K_u} = \frac{1}{K}(P - \alpha p_u), \tag{1.145}$$

and therefore,

$$p_u = \frac{K_u - K}{\alpha K_u}P, \tag{1.146}$$

$$p_u = \frac{K - K_u}{\alpha}\varepsilon_{kk}. \tag{1.147}$$

Equation (1.146) can be used to define the Skempton coefficient B:

$$p_u = BP, \tag{1.148}$$

$$B \equiv \left(\frac{\partial p}{\partial P}\right)_{m,T}, \tag{1.149}$$

$$B = \frac{K_u - K}{\alpha K_u} = \frac{1 - K/K_u}{1 - K/K_S}. \tag{1.150}$$

As $K_S \geq K_u \geq K$, $0 \leq B \leq 1$, and $0 \leq p_u \leq P$. The Skempton coefficient can be used to determine the effect of a change of the confining pressure on a change on the fluid pressure in undrained conditions. Two extreme cases can be considered. When $K_u \to K$, we have $B \to 0$, for instance, when gas is present in the pore space of the porous material. In this case, an increase of the confining pressure has no effect on the fluid pressure because of the very high compressibility of the gas. The second case is when $K \to 0$, $K \ll (K_S, K_u)$. In this case, we have $(\alpha, B) \to 1$. This is the case of a very compressible soil with a very incompressible fluid like water.

To understand the implication of the drained and undrained regimes in terms of deformation, we can think about a tank filled by a water-saturated sand. We apply at $t = 0$ a mechanical load on the top of the sand (think about a building built very quickly on a porous soil). The deformation that follows can be considered using two steps: in the first step, the deformation is instantaneous and undrained with a bulk modulus K_u and a shear modulus G. In this step, we can compute the undrained fluid pressure everywhere, and the fluid has no time to move. In the second step, the fluid starts to flow in response to the generated (undrained) fluid pressure distribution. This flow is responsible for a delayed mechanical response: the soil creeps over time because of the flow of the pore water until an equilibrium situation is reached. Our poroacoustic analysis was proceeding along the same lines: we first determined the undrained fluid pressure associated with the stress or deformation associated with the propagation of the seismic waves (using an undrained bulk modulus; see Figure 1.19), and then, we let the fluid flows in response to the fluid pressure distribution. The flow of water is responsible for the streaming current density defined as the advective drag of the effective charge density $\hat{Q}_V^0$ contained in the pore water (Figure 1.19).

1.5.4 Wave modes in the pure undrained regime

Before we get into the realm of the dynamic Biot–Frenkel theory, it is instructive to review how the two wave modes (pressure or primary (P-)waves and shear or secondary (S-)waves) are obtained in the elastic case. In elastic media, Hooke's law can be written in two different equivalent forms using the elements of the tensors or the tensors themselves:

$$T_{ij} = \left(K_{\mathrm{u}} - \frac{2}{3}G\right)\varepsilon_{kk}\delta_{ij} + 2G\varepsilon_{ij}, \tag{1.151}$$

$$\mathbf{T} = \lambda_{\mathrm{u}}\mathrm{Tr}(\boldsymbol{\varepsilon})\mathbf{I}_3 + 2G\boldsymbol{\varepsilon}, \tag{1.152}$$

where the Lamé coefficient λ_{u} is given by

$$\lambda_{\mathrm{u}} \equiv K_{\mathrm{u}} - \frac{2}{3}G \tag{1.153}$$

and $\mathbf{I}_3$ denotes the 3×3 identity matrix ($\mathbf{T}$ and $\boldsymbol{\varepsilon}$ denote the stress and deformation tensors). If we define the bulk deformation as

$$\theta \equiv \nabla\cdot\mathbf{u} = \varepsilon_{kk}, \tag{1.154}$$

Hooke's law can be written as

$$\mathbf{T} = \lambda_u\theta\mathbf{I} + 2G\boldsymbol{\varepsilon}. \tag{1.155}$$

In order to find the field equation for the displacement of the solid phase, we need to combine Hooke's law (which is a constitutive equation) with a continuity equation, actually the momentum conservation equation applied to the elastic material. This equation corresponds to Newton's law:

$$\nabla\cdot\mathbf{T} = \rho\frac{\partial^2\mathbf{u}}{\partial t^2}, \tag{1.156}$$

$$T_{ij,j} = \rho\ddot{u}_i, \tag{1.157}$$

where ρ denotes the bulk density of the material.

The divergence of the stress tensor can be computed as follows:

$$T_{ij} = \lambda_u u_{k,k}\delta_{ij} + G\left(u_{i,j} + u_{j,i}\right), \tag{1.158}$$

$$T_{ij,j} = \lambda_u u_{k,ki} + G\left(u_{i,jj} + u_{j,ij}\right), \tag{1.159}$$

$$T_{ij,j} = (\lambda_u + G)u_{j,ij} + Gu_{i,jj}, \tag{1.160}$$

$$T_{ij,j} = (\lambda_u + G)u_{i,jj} + Gu_{j,ji}. \tag{1.161}$$

After straightforward algebraic manipulations using the properties of the Kronecker delta and the fact that we can change the order of the derivatives, we obtain

$$\left(\frac{\lambda_u + G}{\rho}\right)u_{j,ji} + \left(\frac{G}{\rho}\right)u_{i,jj} = \ddot{u}_i. \tag{1.162}$$

Equation (1.162) can be written in vectorial notations as

$$\left(\frac{\lambda_u + G}{\rho}\right)\nabla(\nabla\cdot\mathbf{u}) + \left(\frac{G}{\rho}\right)\nabla^2\mathbf{u} = \ddot{\mathbf{u}}. \tag{1.163}$$

Using the general property

$$\nabla^2\mathbf{u} = \nabla(\nabla\cdot\mathbf{u}) - \nabla\times\nabla\times\mathbf{u}, \tag{1.164}$$

we obtain

$$\left(\frac{\lambda_u + 2G}{\rho}\right)\nabla(\nabla\cdot\mathbf{u}) - \left(\frac{G}{\rho}\right)\nabla\times\nabla\times\mathbf{u} = \ddot{\mathbf{u}}. \tag{1.165}$$

Now, we define the following two parameters:

$$c_{\mathrm{p}}^2 = \frac{\lambda_{\mathrm{u}} + 2G}{\rho}, \tag{1.166}$$

$$c_{\mathrm{S}}^2 = \frac{G}{\rho}. \tag{1.167}$$

From Equations (1.165)–(1.167), we have

$$c_{\mathrm{p}}^2\nabla(\nabla\cdot\mathbf{u}) - c_{\mathrm{S}}^2\nabla\times\nabla\times\mathbf{u} = \ddot{\mathbf{u}}. \tag{1.168}$$

Equation (1.168) corresponds to the wave equation of elasticity. To find the different wave modes, we need to use a Helmholtz decomposition of the displacement field:

$$\mathbf{u} = \nabla\varphi + \nabla\times\boldsymbol{\Psi}, \tag{1.169}$$

$$\nabla\cdot\boldsymbol{\Psi} = 0, \tag{1.170}$$

where φ is a scalar potential and $\boldsymbol{\Psi}$ is a vectorial potential. Equation (1.170) corresponds to the so-called coulomb gauge. The Helmholtz decomposition of a vector field

consists in writing this field as the sum of the gradient of a scalar potential and the curl of a vector potential. Using Equations (1.169) and (1.170) in Equation (1.168) and using the properties

$$\nabla\cdot(\nabla\times\Psi)=0, \tag{1.171}$$

$$\nabla\times(\nabla\varphi)=0, \tag{1.172}$$

we end up with two equations:

$$c_{\mathrm{p}}^2\nabla^2\varphi=\ddot{\varphi}, \tag{1.173}$$

$$c_{\mathrm{S}}^2\nabla^2\Psi=\ddot{\Psi}. \tag{1.174}$$

The first mode corresponds to the compressional wave with velocity c_{p}, while the second mode corresponds to the shear mode with velocity c_{S}. The velocity ratio is such that we have

$$\frac{c_{\mathrm{p}}}{c_{\mathrm{S}}}=\sqrt{2+\frac{\lambda_{\mathrm{u}}}{G}}\geq 1. \tag{1.175}$$

Therefore, the P-wave propagates faster than the shear wave. We will show in the next chapters that there are more than two wave modes in poroelastic media. The different wave modes have different EM signatures in seismoelectric theory, and we will discuss in the next chapters these different signatures and their potential applications to probe the Earth using the seismoelectric method.

1.6 Short history

Now that we have discussed some of the key concepts required to understand the seismoelectric theory, we can provide a short introduction to the history of the seismoelectric method. The physics of the streaming potential takes its roots in the experimental work done initially by Quincke (1859) who discovered that the flow of water through a capillary generates a measurable difference of electrical potential. Helmholtz (1879) obtained theoretical expressions for the streaming current density for glass capillaries. The first observations of the seismoelectric effect itself were made by Thompson (1936). Thompson was a geophysicist working for the Humble Oil and Refining Company. His work on the so-called "seismic electric" effect was inspired by Louis Statham in the same company (see Blau & Staham, 1936). They made indeed the first documented observations of electric potential changes between a pair of electrodes when seismic waves passed through these electrodes. Thompson (1936) was looking for the effect of seismic waves on the electrical resistivity of Earth materials. His goal was to detect seismic waves by measuring continuously the electrical resistivity between a set of electrodes. His paper starts as follows: "The seismic electric effect is the name which has been given to the variation of earth resistivity with elastic deformation." The concept of "seismic electric" effect was modeled in the same issue of *Geophysics* by Slotnick (1936) on the base of an equivalent electrical circuit. In the case of Thompson (1936), he measured clear fluctuations in the electrical potentials that could not be explained by a change in the value of the resistance (or apparent resistivity) between the electrodes. In these works, there were no concept that the propagation of the seismic waves could create a source current density or an electrical field on their own and no ideas related to electrokinetic effects and the associated electrical double layer theory.

Ivanov (1939) was the first to record seismoelectric effects in USRR completely passively (no current injection). His pioneering work was followed few years later by the seminal paper of Frenkel (1944). Frenkel developed the first electrokinetic theory of the coseismic electric field in water-saturated porous rocks to explain the observations made by Ivanov. Ivanov and Frenkel should be therefore considered as the pioneers of the seismoelectric method in geophysics. A rigorous treatment of wave propagation in water-saturated porous media was, however, only introduced more than a decade later by Biot (1962a, b). A huge number of field and theoretical works were done in USRR after WWII in using the seismoelectric effect to determine the thickness of the weathered zone to help in interpreting seismic data or for mineral exploration.

Decades after, Frenkel (1944) and Thompson and Gist (1991, 1993) presented a case study for the exploration of oil and gas reservoirs using seismoelectric converted electrical signals. They used adapted data processing and common midpoint (CMP) techniques to produce a seismoelectric image of the subsurface to depths on the order of a few hundred meters. They concluded that seismoelectric conversions could be detected from a depth of 300 m. Thompson and Gist (1993) suggested

that these methods could be used for much greater depths (several kilometers in the case of the electroseismic method). The seismoelectric method has also been used for a variety of applications in near-surface geophysics (for instance, Migunov & Kokorev, 1977; Fourie, 2003; Kulessa et al., 2006). Mikhailov et al. (2000) described crosshole seismoelectric measurements in a small-scale laboratory experiment with vertical and inclined fractures located between the source and the receivers. They recorded not only the coseismic electric signals generated by the seismic wave arriving at the receivers but also the EM wave associated with the Stoneley wave excited in the fracture. They claimed that a tomography image with the travel times extracted from the seismoelectric measurements could be possibly constructed.

Several modeling attempts have been developed to comprehend both the seismoelectric and electroseismic effects. Neev and Yeatts (1989) developed a theory of these effects, but as discussed by Pride (1994), this theory was incomplete. The model developed in the seminal paper of Pride (1994) couples fully the Biot–Frenkel theory to the Maxwell equations via a source current density of electrokinetic origin. This model was obtained by volume averaging the local Navier–Stokes and Nernst–Planck equations as well as the Maxwell equations. It has opened the door to numerical modeling of both the coseismic and seismoelectric conversions using finite-difference or finite-element methods and was used to assess the usefulness of these methods for various applications (e.g., White, 2005; White & Zhou, 2006). The model introduced by Pride has been the fundamental tool used to model the electroseismic and seismoelectric responses of porous rocks in the last two decades (see Haartsen & Toksoz, 1996; Haartsen & Pride, 1997; Garambois & Dietrich, 2001, 2002, for some examples). This approach is however open to some criticisms as discussed later in this book in Chapter 2. Pride's model is unable to describe correctly the surface conductivity, the frequency dependence of the conductivity of the material, and the quadrature conductivity of porous rocks. It is not based on the electrical double layer theory (only the diffuse layer is accounted for), and therefore, some fundamental elements are missing in this theory. That said, Pride has been the first to provide the complete set of macroscopic equations, and his model can easily be corrected to account for the missing components (induced polarization and frequency dependence of the electrical conductivity).

Various authors have used the finite-difference technique to simulate the 2D seismoelectric response of a heterogeneous medium, taking into account all the poroelastic wave modes (fast and slow P-waves and shear (S-)wave) and their coseismic electrical signals plus the seismoelectric conversions (note that the isochoric shear wave does not produce any coseismic electrical field in perfectly homogeneous porous media). Pain et al. (2005) presented a 2D mixed finite-element algorithm to solve the poroelastic Biot equations including the electrokinetic coupling in order to study the sensitivity of the seismoelectric method to material properties, like porosity and permeability of geological formations surrounding a borehole.

Several works have focused on producing some full waveform modeling of the seismoelectric signals using Pride's theory (see, for instance, Grobbe et al., 2012; Grobbe & Slob, 2013). The code developed by Niels Grobbe, electroseismic and seismoelectric modeling (ESSEMOD), is able to model all existing seismoelectric source–receiver combinations (using Pride's theory) in layered media, considering fully coupled Maxwell equations. This code can be also used to model seismoelectric laboratory configurations of a sample in a water tank (i.e., fluid/porous medium/fluid transitions; see Smeulders et al., 2014). This code can also be used to generate all required fields for the theoretical interferometric seismoelectric Green's function retrieval. This allows, for instance, to improve the signal-to-noise ratio of the weak seismoelectric conversions (or interface response fields). By applying interferometric techniques (e.g., Schoemaker et al., 2012), stacking inherently takes place with possible signal-to-noise ratio improvements as well. Along a similar idea, Sava and Revil (2012) introduced recently a simplified poroacoustic formulation to describe the seismoelectric coupling in porous media, and they introduce a new method called seismoelectric beamforming. The idea is to focus seismic waves on a grid of specific points and to use the seismoelectric conversion to image heterogeneities in mechanical and electrical properties (see Chapter 6). The poroacoustic approximation allows handling the computation of the seismoelectric signals in very complex geometries very quickly, and the beamforming approach is used to enhance the seismoelectric conversion over the coseismic signals.

Most of the current efforts in seismoelectric theory are also directed to understand the seismoelectric conversions in unsaturated or in porous media saturated by

two immiscible fluid phases. In most cases, the water-saturated case is extended to unsaturated flow assuming that the nonwetting fluid is air at atmospheric pressure and corresponds to a very compressible phase (Revil et al., 2014). Recently, Smeulders et al. (2014) have used Pride's model to perform laboratory experiments between water and water-saturated core samples or oil-saturated core samples. They found that the contrast between water and water-saturated porous glass samples is larger than the contrast between water and oil-saturated porous glass samples. The contrast between water and water-saturated Fontainebleau sandstone is observed to be larger than the contrast between oil and water-saturated Fontainebleau sandstone in agreement with the models of Revil and Mahardika (2013) and Revil et al. (2014). A complete theory of the seismoelectric conversions in porous media saturated by two immiscible fluids will be given in this book in Chapter 3.

In parallel to the history of the seismoelectric method in geophysics, there is a rich history in the development of the so-called electroacoustic spectroscopic methods to study colloidal suspensions, concentrated dispersion, emulsions, and microemulsions (Booth & Enderly, 1952; Marlow et al., 1983; Valdez, 1993). Debye (1933) predicted that the passage of an acoustic wave through an electrolyte would generate an electrical field, the so-called ion vibration potential (IVP). Indeed, as a sound wave passes through a solution, it is responsible for a charge separation due to differences in the effective masses and frictional coefficients of the solvated anions and cations. The resulting sum of these tiny dipoles leads to a macroscopic electrical field, which depends on the sound wave frequency. This effect was observed a decade later by Yaeger et al. (1949) and Derouet and Denizot (1951).

Hermans (1938) and Rutgers et al. (1958) were the first to report a colloid vibration potential (CVP), investigating therefore the electrical field associated with the passage of acoustic waves through a colloidal suspension. Colloidal suspensions represent a suspension of very small solid particles (less than few micrometers) in water. They can be understood, therefore, as a special case of very high-porosity porous media. Generally speaking, CVP and colloid vibration current (CVI) are two phenomena where acoustic waves are applied to a colloidal system and a resultant electric field or current is created by the vibration of the colloid electric double layers. Several hundred of experimental and theoretical works have been published in this field since the 1950s. For brevity, we mention here only a few key papers. Enderby (1951) and Booth and Enderby (1952) developed the first theory for CVP in the early 1950s. The first quantitative experiments were made in the 1960s by Zana and Yeager (1967a, b, c, 1982). Oja et al. (1985) observed an inverse electroacoustic effect called the electrosonic amplitude (ESA). ESA involves the generation of acoustic waves caused by the driving force of an applied electric field or electrical current and is therefore associated with electroosmotic effects (i.e., the movement of the water in response to an electrical field due to the excess of charge present in the pore water). It is however nothing else than electroseismic effects in the wording commonly used in geophysics.

The first commercially available electroacoustic instruments were developed by Pen Kem, Inc. (Marlow et al., 1990). There are now several commercially available instruments manufactured by Colloidal Dynamics, Dispersion Technology, and Matec. The electroacoustic spectroscopic methods are used to determine the particle size distribution as well as the zeta potential of the particles. Like the seismoelectric and electroseismic methods, there are two different electroacoustic methods depending on what field is used as a driving force. CVI is the phenomenon where acoustic waves are applied to a system and a resultant electric field or current is created by the vibration of the colloid electric double layers. Scales and Jones (1992) were the first to recognize the effect of polydispersity (particle size distribution) on the electroacoustic measurements. A comprehensive theory was developed by O'Brien (1991) and O'Brien et al. (1993) including for concentrated systems, that is, relatively low-porosity materials. A review of the method can be found in Hunter (1998) and Greenwood (2003).

1.7 Conclusions

We summarize the ideas developed in this chapter as follows: (1) the surface of minerals in contact with water is charged. This charge is compensated by a charge in the pore water, which is therefore not neutral in proximity to the mineral grain surface. The surface charge of the minerals is counterbalanced locally by ions that are sorbed (and therefore "attached" to the mineral surface), forming the Stern layer and some ions forming a diffuse layer that interacts with the mineral surface charge only

through the coulombic interaction. (2) The flow of pore water with respect to the solid phase (formed by the assemblage of grains) generates a source current density due to the drag of the charge density, near the mineral grain surface, contained in the pore water. This streaming current depends on either the zeta potential, ζ, or an effective charge density $\hat{Q}_V^0$. We established a bridge between these two quantities. (3) The seismoelectric response due to the flow of water relative to the mineral framework is triggered by the propagation of seismic waves and, possibly as discussed later in Chapter 5, by the seismic source itself. We must therefore account for three types of EM disturbances: those associated with the seismic sources, the coseismoelectric effects associated with the propagation of the seismic waves, and the seismoelectric conversion (also called interface response) associated with the conversion of hydromechanical to EM energy at macroscopic interfaces in the investigated material. (4) The distribution of the resulting electrical field is controlled not only by the source current density (direction and magnitude) generated in the porous material but also by the conductivity distribution in the material. This conductivity is frequency dependent (to some extent) and is characterized by both an inphase component and a quadrature component. This implies that the electrical field is not necessarily in phase with the source current density. The frequency dependence of the electrical conductivity is termed induced polarization in geophysics and is not captured by the theory of Pride.

We have also discussed previously the main ingredients that are necessary to set the stage for the introduction of the seismoelectric method. Chapter 2 will be devoted to the development of a seismoelectric theory in fully water-saturated conditions. This requires discussion of the equations describing the propagation of seismic waves in porous media characterized by a linear elastic skeleton (dynamic poroelasticity) and the Maxwell equations, usually taken in their quasistatic forms.

References

Ahmad, M.U. (1969) A laboratory study of streaming potentials. *Geophysical Prospecting*, **12**(**1**), 49–64.

Avena, M.J. & De Pauli, C.P. (1998) Proton adsorption and electrokinetics of an Argentinean Montmorillonite. *Journal of Colloid and Interface Science*, **202**, 195–204, doi: 10.1006/jcis.1998.5402.

Biot, M.A. (1962a) Generalized theory of acoustic propagation in porous dissipative media. *Journal of the Acoustical Society of America*, **34**(**9**), 1254–1264.

Biot, M.A. (1962b) Mechanics of deformation and acoustic propagation in porous media. *Journal of Applied Physics*, **33**(**4**), 1482–1498.

Blau, L. & Statham, L. (1936) Method and apparatus for seismic electric prospecting. Technical Report, 2054067, U.S. Patent and Trademark Office (USPTO), Washington, DC.

Bolève, A., Crespy, A., Revil, A., Janod, F., & Mattiuzzo J.L. (2007) Streaming potentials of granular media: Influence of the Dukhin and Reynolds numbers. *Journal of Geophysical Research*, **112**, B08204, doi:10.1029/2006JB004673.

Booth, F. & Enderby, J. (1952) On electrical effects due to sound Waves in Colloidal Suspensions. *Proceedings of the American Physical Society*, **208A**, 32–42.

Börner, F.D. (1992) Complex conductivity measurements of reservoir properties. Proceedings of the Third European Core Analysis Symposium, Paris, 359–386.

Casagrande, L. (1983) Stabilization of soils by means of electro-osmosis: State of art. *Journal of Boston Society of Civil Engineers*, **69**(**2**), 255–302.

Chapman, D.L. (1913) A contribution to the theory of electrocapillarity. *Philosophical Magazine*, **25**(**6**), 475–481.

Chittoori, B. & Puppala, A.J. (2011) Quantitative estimation of clay mineralogy in fine-grained soils. *Journal of Geotechnical and Geoenvironmental Engineering*, **137**(**11**), 997–1008, doi: 10.1061/(ASCE)GT.1943-5606.0000521.

Cicerone, D.S., Regazzoni, A.E., & Blesa, M.A. (1992) Electrokinetic properties of the calcite/water interface in the presence of magnesium and organic matter. *Journal of Colloid and Interface Science*, **154**, 423–433.

Darcy, H. (1856) *Les fontaines publiques de la Ville de Dijon*, Dalmont, Paris.

Debye, P. (1933) A method for the determination of the mass of electrolyte ions. *Journal of Chemical Physics*, **1**, 13–16.

Derouet, B. & Denizot, F. (1951) Comptes Rendus de l'Académie des Sciences, *Paris*, **233**, 368.

Einstein, A. (1916) The foundations of the general theory of relativity. *Annalen der Physik*, **354**(**7**), 769–822, doi:10.1002/andp.19163540702.

Enderby, J.A. (1951) On electrical effects due to sound waves in colloidal suspensions. *Proceedings of the Royal Society, London*, **A207**, 329–342.

Fourie, F.D. (2003) Application of Electroseismic Techniques to Geohydrological Investigations in Karoo Rocks, PhD Thesis, University of the Free State, Bloemfontein, South Africa, 195 pp.

Frenkel, J. (1944) On the theory of seismic and seismoelectric phenomena in a moist soil, *Journal Physics (Soviet)*, **8**(**4**), 230–241.

Friborg, J. (1996) Experimental and theoretical investigations into the streaming potential phenomenon with special

reference to applications in glaciated terrain. PhD thesis, Lulea University of Technology, Sweden.

Garambois, S. & Dietrich, M. (2001) Seismoelectric wave conversions in porous media: field measurements and transfer function analysis. *Geophysics*, **66**(**5**), 1417–1430.

Garambois, S. & Dietrich, M. (2002) Full waveform numerical simulations of seismoelectromagnetic wave conversions in fluid-saturated stratified porous media. *Journal of Geophysical Research*, **107**(**B7**), ESE5-1–ESE5-18.

Gassmann, F. (1951) Über die elastizität poröser medien. *Vierteljahrsschrift der Naturforschenden Gesellschaft Zuerich*, **96**, 1–23.

Gaudin, A. M. & Fuerstenau, D.W. (1955) Quartz flotation with anionic collectors *Transactions of the American Institute of Mining, Metallurgical, and Petroleum Engineers*, **202**, 66–72.

Gonçalvès, J., Rousseau-Gueutin, P., & Revil, A. (2007) Introducing interacting diffuse layers in TLM calculations: a reappraisal of the influence of the pore size on the swelling pressure and the osmotic efficiency of compacted bentonites. *Journal of Colloid and Interface Science*, **316**, 92–99.

Gouy, G.L. (1910) Sur la constitution de la charge électrique à la surface d'un électrolyte. *Journal de Physique Théorique et Appliquée*, **9**(**4**), 457–468.

Greenwood, R. (2003) Review of the measurement of zeta potentials in concentrated aqueous suspensions using electroacoustics. *Advances in Colloid and Interface Science*, **106**, 55–81, doi:10.1016/S0001-8686(03)00105-2.

Grobbe, N. & Slob, E. (2013) Validation of an electroseismic and seismoelectric modeling code, for layered earth models, by the explicit homogeneous space solutions. In: *SEG Technical Program Expanded Abstracts*, Society of Petroleum Geologists, Houston. pp. 1847–1851.

Grobbe, N., Thorbecke, J., & Slob, E. (2012) ESSEMOD—electroseismic and seismoelectric flux-normalized modeling for horizontally layered, radially symmetric configurations. *Geophysical Research Abstract*, **14**:10011.

Grosse, C. (2009) Generalization of a classic theory of the low frequency dielectric dispersion of colloidal suspensions to electrolyte solutions with different ion valences. *Journal of Physical Chemistry B*, **113**, 11201–11215.

Haartsen, M.W. & Pride, S.R. (1997) Electroseismic waves from point sources in layered media. *Journal of Geophysical Research*, **102**(**B11**), 24 745–24 769.

Haartsen, M. W. & Toksoz, M. N. (1996) Dynamic streaming currents from seismic point sources in homogeneous poroelastic media. *Geophysical Journal International*, **132**, 256– 274.

Hermans, J. (1938) Charged colloid particles in an ultrasonic field. *Philosophical Magazine*, **25**, 426.

Helmholtz, H. (1879) Study concerning electrical boundary boundary layers. *Weidemann Annal Physik Chemie*, **7**, 337–382, 3rd Ser.

Hiorth, A., Cathles, L.M., & Madland, M.V. (2010) The impact of pore water chemistry on carbonate surface charge and oil wettability. *Transport in Porous Media*, **85**(**1**), 1–21.

Hunt, A., Huisman, J.A. & Vereecken, H. (2012) On the origin of slow processes of charge transport in porous media. *Philosophical Magazine*, **92**(**36**), 4628–4648.

Hunter, R.J. (1981) *Zeta Potential in Colloid Science: Principles and Applications*, Academic Press, New York.

Hunter R.J. (1998) Review recent developments in the electroacoustic characterisation of colloidal suspensions and emulsions. *Colloids Surface A*, **141**, 37–65.

Ivanov, A. G. (1939) Effect of electrization of earth layers by elastic waves passing through them. *Proceedings of the USSR Academy of Sciences (Dokl. Akad. Nauk SSSR)*, **24**, 42–45.

Jaafar, M. Z., Vinogradov, J., & M. D. Jackson (2009) Measurement of streaming potential coupling coefficient in sandstones saturated with high salinity NaCl brine. *Geophysical Research Letters*, **36**, L21306, doi:10.1029/2009GL040549.

Jardani, A., Revil, A., Bolève, A., Dupont, J.P., Barrash, W., & Malama B (2007) Tomography of groundwater flow from self-potential (SP) data. *Geophysical Research Letters*, **34**, L24403.

Jougnot, D., Revil, A., & Leroy P. (2009) Diffusion of ionic tracers in the Callovo-Oxfordian clay-rock using the Donnan equilibrium model and the electrical formation factor. *Geochemica et Cosmochemica Acta*, **73**, 2712–2726.

Jougnot, D., Linde, N., Revil, A., & Doussan, C. (2012) Derivation of soil-specific streaming potential electrical parameters from hydrodynamic characteristics of partially saturated soils. *Vadoze Zone Journal*, **11**(**1**), 1–15, doi:10.2136/vzj2011.0086.

Kitamura, A., Fujiwara, K., Yamamoto, T., Nishikawa, S., & Moriyama, H. (1999) Analysis of adsorption behavior of cations onto quartz surface by electrical double-layer model, *Journal of Nuclear Science and Technology*, **36**, 1167–1175.

Koch, K., Kemna, A., Irving, J., & Holliger, K. (2011) Impact of changes in grain size and pore space on the hydraulic conductivity and spectral induced polarization response of sand. *Hydrological Earth System Science*, **15**, 1785–1794, doi:10.5194/hess-15-1785-2011

Koch, K., Revil, A. & Holliger, K. (2012) Relating the permeability of quartz sands to their grain size and spectral induced polarization characteristics. *Geophysical Journal International*, **190**, 230–242, doi: 10.1111/j.1365-246X.2012.05510.x.

Kulessa, B., Murray, T. & Rippin, D. (2006) Active seismoelectric exploration of glaciers. *Geophysical Research Letters*, **33**, L07503, doi:10.1029/2006GL025758.

Leroy, P. & Revil A. (2004) A triple layer model of the surface electrochemical properties of clay minerals. *Journal of Colloid and Interface Science*, **270**(**2**), 371–380.

Leroy, P., Revil, A., Altmann, S., & Tournassat, C. (2007) Modeling the composition of the pore water in a clay-rock geological formation (Callovo-Oxfordian, France). *Geochimica et Cosmochimica Acta*, **71**(**5**), 1087–1097, doi: 10.1016/j.gca.2006.11.009.

Leroy, P., Revil, A., Kemna, A., Cosenza, P., & Ghorbani, A. (2008) Spectral induced polarization of water-saturated packs of glass beads. *Journal of Colloid and Interface Science*, **321**(**1**), 103–117.

Lesmes, D.P. & Frye, K.M. (2001) Influence of pore fluid chemistry on the complex conductivity and induced polarization responses of Berea sandstone. *Journal of Geophysical Research*, **106**(**B3**), 4079–4090.

Li, H.C. & De Bruyn, P.L. (1966) Electrokinetic and adsorption studies on quartz. *Surface Science*, **5**, 203–220.

Lipsicas, M. (1984) Molecular and surface interactions in clay intercalates, in *Physics and Chemistry of Porous Media*, edited by D. L. Johnson and P. N. Sen, eds., pp. 191–202, American Institute of Physics, College Park.

Lockhart, N. C. (1980) Electrical properties and the surface characteristics and structure of clays, II, Kaolinite: a nonswelling clay. *Journal of Colloid and Interface Science*, **74**, 520–529.

Lorne, B., Perrier, F., & Avouac, J.-P. (1999a) Streaming potential measurements. 1. Properties of the electrical double layer from crushed rock samples. *Journal of Geophysical Research*, **104**(**B8**), 17857–17877.

Lorne, B., Perrier, F., & Avouac, J.-P. (1999b) Streaming potential measurements. 2. Relationship between electrical and hydraulic flow patterns from rocks samples during deformations. *Journal of Geophysical Research*, **104**(**B8**), 17,879–17,896.

Ma, C. & Eggleton, R. A. (1999) Cation exchange capacity of kaolinite. *Clays and Clay Minerals*, **47**, 174–180.

Maes, A., Stul, M.S. & Cremers, A. (1979) Layer charge-cation-exchange capacity relationships in montmorillonite, *Clays and Clay Minerals*, **27**, 387–392.

Marlow, B.J., Fairhurst, D., & Pendse, H.P. (1983) Colloid vibration potential and the electrokinetic characterization of concentrated colloids. *Langmuir*, **4**(**3**), 611–626.

Marlow, B.J., Oja, T., & Goetz, P.J. (1990) Colloid Analyzer, U.S. Patent 4,907,453.

Marshall, D. J. & Madden, T. R. (1959) Induced polarization, a study of its causes. *Geophysics*, **24**, 790–816.

Migunov, N. & Kokorev, A. (1977) Dynamic properties of the seismoelectric effect of water saturated rocks. *Izvestiya, Earth Physics*, **13**(**6**), 443–446.

Mikhailov, O.V., Queen, J. & Toksoz, M.N. (2000) Using borehole electroseismic measurements to detect and characterize fractured (permeable) zones. *Geophysics*, **65**(**4**), 1098–1112, doi:10.1190/1.1444803.

Neev, J. & Yeatts, F.R. (1989) Electrokinetic effects in fluid-saturated poro-elastic media, *Physical Review B*, **40**(**13**), 9135–9141.

O'Brien, R.W. (1991) Determination of Particle Size and Electric Charge, U.S. Patent 5,059,909, October 22, 1991.

O'Brien, R.W., Rowlands, W.N., & Hunter R.J. (1993) Determining charge and size with the acoustosizer, in: National Institute of Standards and Technology Special Publication 856, tric point. USA Department of Commerce, Washington, DC, pp. 1–22.

Oja, T., Petersen, G., & Cannon, D. (1985) Measurement of electric-kinetic properties of a solution. U.S. Patent 4,497,208.

Pain, C.C., Saunders, J.H., Worthington, M.H. et al. (2005) A mixed finite-element method for solving the poroelastic Biot equation with electrokinetic coupling. *Geophysical Journal of International*, **160**, 592–608.

Patchett, J. G. (1975) An investigation of shale conductivity, Society of Professional Well Logging Analysis 16th Logging Symposium, Paper U, Houston, TX, 41 pp.

Pengra, D.B., Li, S.X., & Wong P.-Z. (1999) Determination of rock properties by low-frequency AC electrokinetics. *Journal of Geophysical Research*, **104**(**B12**), 29485–29508.

Poley, J.P., Nooteboom, J.J. & de Waal, P.J. (1978) Use of V.H.R. dielectric measurements for borehole formation analysis. *The Log Analyst*, **19**(**3**), 8–30.

Pride, S. (1994) Governing equations for the coupled electromagnetics and acoustics of porous media. *Physical Review B*, **50**, 15678–15696.

Pride, S. & Morgan, F.D. (1991) Electrokinetic dissipation induced by seismic waves. *Geophysics*, **56**(**7**), 914–925.

Quincke, G. (1859) Concerning a new type of electrical current. *Annalen der Physics und Chemie (Poggendorff's Annal., Ser. 2)*, **107**, 1–47.

Revil, A., Schwaeger, H., Cathles, L.M., & Manhardt, P. (1999a) Streaming potential in porous media. 2. Theory and application to geothermal systems. *Journal of Geophysical Research*, **104**(**B9**), 20033–20048.

Revil, A., Pezard, P.A., & Glover, P.W.J. (1999b) Streaming potential in porous media. 1. Theory of the zeta-potential. *Journal of Geophysical Research*, **104**(**B9**), 20021–20031.

Revil, A., Leroy, P., & Titov, K. (2005) *Characterization of transport properties of argillaceous sediments. Application to the Callovo-Oxfordian Argillite. Journal of Geophysical Research*, **110**, B06202, doi: 10.1029/2004JB003442.

Revil, A., Linde, N., Cerepi, A., Jougnot, D., Matthäi, S., & Finsterle, S. (2007) Electrokinetic coupling in unsaturated porous media, *Journal of Colloid and Interface Science*, **313**(**1**), 315–327, doi:10.1016/j.jcis.2007.03.037.

Revil, A. & Florsch, N. (2010) Determination of permeability from spectral induced polarization data in granular media, *Geophysical Journal International*, **181**, 1480–1498, doi: 10.1111/j.1365-246X.2010.04573.

Revil A. & Jardani, A. (2010) Seismoelectric response of heavy oil reservoirs. Theory and numerical modelling. *Geophysical Journal International*, **180**, 781–797, doi: 10.1111/j.1365-246X.2009.04439.x.

Revil, A. & Skold, M. (2011) Salinity dependence of spectral induced polarization in sands and sandstones. *Geophysical Journal International*, **187**, 813–824, doi: 10.1111/j.1365-246X.2011.05181.x.

Revil, A., Karaoulis, M., Johnson, T., & Kemna, A. (2012) Review: Some low-frequency electrical methods for subsurface characterization and monitoring in hydrogeology, *Hydrogeology Journal*, **20**(**4**), 617–658, doi:10.1007/s10040-011-0819-x, 2012.

Revil, A. (2012) Spectral induced polarization of shaly sands: Influence of the electrical double layer. *Water Resources Reseacrh*, **48**, W02517, doi:10.1029/2011WR011260.

Revil, A. & H. Mahardika (2013) Coupled hydromechanical and electromagnetic disturbances in unsaturated clayey materials. *Water Resources Research*, **49**, doi:10.1002/wrcr.20092.

Revil, A., Skold, M., Hubbard, S.S., Wu, Y., Watson, D., & Karaoulis, M. (2013) Petrophysical properties of saprolites from the Oak Ridge Integrated Field Research Challenge site, Tennessee. *Geophysics*, **78**(**1**), D21–D40, doi: 10.1190/geo2012-0176.1.

Revil, A. (2013a) Effective conductivity and permittivity of unsaturated porous materials in the frequency range 1 mHz–1GHz. *Water Resources Research*, **49**, doi:10.1029/2012WR012700.

Revil, A. (2013b) On charge accumulations in heterogeneous porous materials under the influence of an electrical field. *Geophysics*, **78**(**4**), D271–D291, doi: 10.1190/GEO2012-0503.1.

Revil A., Barnier, G., Karaoulis, M., & Sava, P. (2014) Seismoelectric coupling in unsaturated porous media: theory, petrophysics, and saturation front localization using an electroacoustic approach. *Geophysical Journal International*, **196**(**2**): 867–884, doi: 10.1093/gji/ggt440.

Rutgers, A.J. & Rigole, W. (1958) Ultrasonic vibration potentials in colloid solutions, in solutions of electrolytes and pure liquids, *Transactions of the Faraday Society*, **54**, 139–143.

Sava, P. & Revil, A. (2012) Virtual electrode current injection using seismic focusing and seismoelectric conversion. *Geophysical Journal International*, **191**(**3**), 1205–1209, doi: 10.1111/j.1365-246X.2012.05700.x.

Scales P.J. & Jones, E. (1992) Effect of particle size distribution on the accuracy of electroacoustic mobilities. *Langmuir*, **8**(**2**), 385–389.

Schmutz, M., Revil, A., Vaudelet, P., Batzle, M., Femenia Vinao, P., & Werkema, D.D. (2010) Influence of oil saturation upon spectral induced polarization of oil bearing sands. *Geophysical Journal International*, **183**, 211–224, doi:10.1111/j.1365-246X.2010.04751.x.

Schoemaker, F.C., Grobbe, N., Schakel, M. D., de Ridder, S. A. L. and Slob, E. C. & Smeulders, D. M. J. (2012) Experimental validation of the electrokinetic theory and development of seismoelectric interferometry by cross-correlation. *International Journal of Geophysics*, **514242**, 23 pp., doi:10.1155/2012/514242.

Shainberg, I., Alperovitch, N. & Keren, R. (1988) Effect of magnesium on the hydraulic conductivity of Na-smectite-sand mixtures. *Clays and Clay Minerals*, **36**, 432– 438.

Sheffer, M.R. (2007) Forward modeling and inversion of streaming potential for the interpretation of hydraulic conditions from self-potential data. PhD thesis, University of British Columbia.

Sinitsyn, V. A., S. U. Aja, D. A. Kulik, & S. A. Wood (2000) Acid-base surface chemistry and sorption of some lanthanides on K^+-saturated Marblehead illite. I. Results of an experimental investigation. *Geochimica et Cosmochimica Acta*, **64**, 185–194.

Slater, L.D. & Glaser, D.R. (2003) Controls on induced polarization in sandy unconsolidated sediments and application to aquifer characterization. *Geophysics*, **68**(**5**), 1547–1558, doi: 10.1190/1.1620628.

Slater, L. & Lesmes, D. P. (2002) Electrical-hydraulic relationships observed for unconsolidated sediments. *Water Resources Research*, **38**(**10**), 1213, doi: 10.1029/2001WR001075.

Slotnick, M.M. (1936) A simplified circuit of the seismic electric method and its steady-state solution. *Geophysics*, **1**, 336–339.

Smeulders, D.M.J., Grobbe, N., Heller, H.K.J., & Schakel, M.D. (2014) Seismoelectric conversion for the detection of porous medium interfaces between wetting and nonwetting fluids. *Vadoze Zone Journal*, **5**, 7 pp, doi:10.2136/vzj2013.06.0106.

Stern, O. (1924) Zur Theorie der elektrolytischen Doppelschicht (The theory of the electrolytic double shift). *Zeitschrift Fur Elektrochemie Und Angewandte Physikalische Chemie*, **30**, 508–516.

Strand, S., Høgnesen, E.J. & Austad, T. (2006) Wettability alteration of carbonates-effects of potential determining ions (Ca and SO4) and temperature. *Colloids and Surfaces A: Physiochemical and Engineering Aspects*, **275**, 1–10.

Su, Q., Feng, Q. & Shang, Z. (2000) Electrical impedance variation with water saturation in rock, *Geophysics*, **65**, 68–75.

Sverjensky, D. A. (2005) Prediction of the speciation of alkaline earths adsorbed on mineral surfaces in salt solutions. *Geochimica et Cosmochimica Acta*, **69**, 225–257.

Tadros, Th.F. & Lyklema J. (1969) The electrical double layer on silica in the presence of bivalent counter-ions. *Journal of Electroanalytical Chemistry, Interfacial and Electrochemistry*, **22**, 1–7.

Terzaghi, K. (1943) *Theoretical Soil Mechanics*. John Wiley & Sons, New York.

Thompson, R.R. (1936) The seismic electric effect. *Geophysics*, **1**, 327–335.

Thompson, A. H. & Gist, G. (1991) Electroseismic prospecting, Society of Exploration Geophysics 61st Annual International Meeting, Expanded Abstracts, Houston, TX, pp. 425–427.

Thompson, A. H. & Gist, G. (1993) Geophysical applications of electrokinetic conversion, *Leading Edge*, **12**, 1169–1173.

Titov, K., Kemna, A., Tarasov, A., & Vereecken, H. (2004) Induced polarization of unsaturated sands determined through time-domain measurements. *Vadose Zone Journal*, **3**, 1160–1168.

Tournassat, C., Ferrage, E., Poinsignon, C., & Charlet L. (2004), The titration of clay minerals. Part II. Structural-based model and implications for clay reactivity. *Journal of Colloid and Interface Science*, **273**, 234–246.

Valdez J.L. (1993) Electroacoustics for characterisation of particulates and suspensions: Proceedings of Workshop Held at the National Institute of Standards and Technology, February 3–4, 1993, Gaithersburg, MD, in: S.G. Malghan (Ed.), US Department of Commerce, Washington, DC, 1993, pp. 111–128, NIST Special publication 856.

van Bekkum, H., Flanigen, E.M., & Jansen J.C. (2001) *Introduction to Zeolite Science and Practice, Studies in Surface Science and Catalysis*, vol. 58, Elsevier, Amsterdam.

Vinegar, H.J. & Waxman, M.H. (1984) Induced polarization of shaly sands. *Geophysics*, **49**, 1267–1287.

von Smoluchowski, M. (1906) Zur kinetischen Theorie der Brownschen Molekularbewegung und der Suspensionen (in German). *Annalen der Physik*, **326**(**14**), 756–780.

Wang, M. & Revil, A. (2010) Electrochemical charge of silica surface at high ionic strength in narrow channels. *Journal of Colloid and Interface Science*, **343**, 381–386, 2010.

Watilllon, A. & De Backer, R. (1970) Potentiel d'écoulement, courant d'coulement et conductance de surface à l'interface eau-verre. *Journal of Electroanalytical Chemistry*, **25**, 181–196.

White, B.S. (2005) Asymptotic Theory of Electroseismic Prospecting. *SIAM Journal of Applied Mathematics*, **65**(**4**), 1443–1462.

White, B.S. & Zhou, M. (2006) Electroseismic prospecting in layered media. *SIAM Journal of Applied Mathematics*, **67**(**1**), 69–98.

Yeager, E., Bugosh, J., Hovorka, F., & McCarthy, J. (1949) The application of ultrasonics to the study of electrolyte solutions. II. The detection of Debye effect. *Journal of chemical Physics*, **17**(**4**), 411–415.

Zana, R. & Yeager, E. (1967a) Quantitative studies of ultrasonic vibration potentials in polyelectrolyte solutions. *The Journal of Physical Chemistry*, **71**(**11**), 3502–3520.

Zana, R. & Yeager, E. (1967b) Ultrasonic vibration potentials in tetraalkylammonium halide solutions. *The Journal of Physical Chemistry*, **71**(**13**), 4241–4244.

Zana, R. & Yeager, E., (1967c) Ultrasonic vibration potentials and their use in the determination of ionic partial molal volumes, *The Journal of Physical Chemistry*, **71**(**13**), 521–535.

Zana, R. & Yeager, E. (1982) Ultrasonic vibration potentials. *Modern Aspects of Electrochemistry*, **14**, 3–60.

Zhu, Z. & Toksöz, M.N. (2013) Experimental measurements of the streaming potential and seismoelectric conversion in Berea sandstone. *Geophysical Prospecting*, **61**(**3**), 688–700, doi: 10.1111/j.1365-2478.2012.01110.

Zundel, J.P. & Siffert, B. (1985) Mécanisme de rétention de l'octylbenzene sulfonate de sodium sur les minéraux argileux. Solid-Liquid Interactions in Porous Media, pp. 447–462, Technip, Paris.